Physics-Based Thermal Reduced-Order Models for Battery Pack Health Monitoring: Application to NASA's X-57 Electric Aircraft

Michael Khasin[a], Mohit R. Mehta[b], John W. Lawson[a]

[a]*NASA, Intelligent Systems Division, NASA Ames Research Center, Moffett Field, 94035, California, U.S.A*
[b]*KBR Inc., Intelligent Systems Division, NASA Ames Research Center, Moffett Field, 94035, California, U.S.A*

Abstract

Prognostics and Health Management (PHM) of large lithium-ion battery packs is critical for electrified aircraft and space systems. Pack-level workflows rely on reduced-order models (ROMs). The dominant equivalent-circuit variants are ad hoc, leaving accuracy and identifiability unverified. Physics-based electro–thermal high-fidelity models (HFMs) are mechanism-rich but severely non-identifiable under sparse sensing. We therefore reformulate a comprehensive HFM of NASA's X-57 Maxwell battery system (nearly 1300 independent parameters) in terms of the sensor variables. We then apply the Adaptive Soft-Mode Manifold Boundary Approximation Method (AS-MBAM), a novel procedure for ROM candidate discovery. AS-MBAM locates candidate limiting models using first-order sensitivities already computed for fitting, whereas MBAM requires second-order derivatives. Following both orientations of the soft mode generates a branching tree of candidates. In a toy model the search yields distinct reduced theories of comparable accuracy: the observations support several effective descriptions. The X-57 reduction yields a five-parameter Thermal Reduced-Order Model (5pTROM) sufficiently identifiable for the present application. Across 256 brick–sensor fits from one laboratory Simulated Flight Profile discharge, most temperature root-mean-square errors are below 0.5 °C. Four fitted parameters per sensor show coherent pack-wide trends; the fifth, B_a, remains sloppy. Future studies will test cross-mission transfer, fault discrimination, and prognostic value.

Keywords: Electro-thermal modeling; Reduced-order modeling; Parameter identifiability; Battery health monitoring; Information geometry.

Nomenclature

Acronyms

AS-MBAM	Adaptive Soft-Mode Manifold Boundary Approximation Method
EAP	Electrified Aircraft Propulsion
ECM	Equivalent Circuit Model
FIM	Fisher Information Matrix
HFM	High-Fidelity Model
Li-ion	Lithium-ion
MBAM	Manifold Boundary Approximation Method
MSE	Mean Square Error
OCP	Open Circuit Potential
PHM	Prognostics and Health Management
RMSE	Root Mean Square Error
ROM	Reduced Order Model
SEI	Solid Electrolyte Interphase
SFP	Simulated Flight Profile
SOC	State of Charge
5pTROM	Five-parameter Thermal Reduced-Order Model

List of Symbols

Symbol	Description	Units
A, B_a, B_c	OCP (open-circuit potential) model parameters ($A = A_c - A_a$)	V
A_a, A_c	Anode/cathode OCP offsets in Ansatz	V
Bi	Biot number	–
$c_{p,\text{eff}}$	Effective specific heat of sub-module	$\mathrm{J\,kg^{-1}\,K^{-1}}$
e	Elementary charge	C
F	Least-squares/Gauss–Newton FIM or sensitivity metric ($F = J^\top J$)	–
Gr	Grashof number	–
$h(t')$	Inverse Laplace kernel of diffusion transfer function	–
h_{conv}	Convective heat transfer coefficient	$\mathrm{W\,m^{-2}\,K^{-1}}$
h_{rad}	Linearized radiation heat transfer coefficient	$\mathrm{W\,m^{-2}\,K^{-1}}$
h_{total}	Total external heat transfer coefficient ($h_{\text{conv}} + h_{\text{rad}}$)	$\mathrm{W\,m^{-2}\,K^{-1}}$
$I(t)$	Cell current (local, unless noted)	A
J	Jacobian of the normalized residual vector with respect to parameters	–
k_{eff}	Effective thermal conductivity (generic)	$\mathrm{W\,m^{-1}\,K^{-1}}$
$k_{\text{eff},\perp}$	Effective conductivity (through thickness)	$\mathrm{W\,m^{-1}\,K^{-1}}$
$k_{\text{eff},\parallel}$	Effective conductivity (in-plane)	$\mathrm{W\,m^{-1}\,K^{-1}}$
L	Number of thermal sensors	–
L_c	Characteristic length (here: sub-module thickness)	m
N	Number of cells in toy model string	–
N_1, N_2	Grid dimensions in sub-module discretization	–
$N_{\text{Li},a}$	Total number of Li ions available for intercalation in anode	–
$N_{\text{Li},c}$	Total number of Li ion intercalation sites in cathode	–
p	Physical parameter vector	mixed
q	Dimensionless relative-parameter vector, $q_i = p_i / p_{0,i}$	–
p_0	Local best-fit parameter vector used for relative scaling	mixed
$Q(t)$	Total charge passed, $\int_0^t I(t')\,dt'$	C
$\tilde{r}$	Effective series resistance	Ω
s	Dimensionless AS-MBAM continuation parameter or pseudo-time	–
ζ	Laplace variable	$\mathrm{s^{-1}}$
T_{ij}	Cell temperature at location (i, j)	K (or °C)
T_{ij}^M	Matrix sub-volume temperature at (i, j)	K (or °C)
$T(t)$	Local (measured) matrix temperature at a sensor	K (or °C)
$\Delta T(t)$	Local measured temperature rise, $T(t) - T(0)$	K (or °C)
$T_{\text{hot}}, T_{\text{cold}}$	Hot surface/ambient temperatures for linearized radiation	K
$V(t)$	Cell terminal voltage	V
$V(0)$	Initial fully charged voltage	V
$\bar{x}_a(t)$	Normalized anode surface intercalation fraction	–
$\bar{x}_c(t)$	Normalized cathode surface intercalation fraction	–
$x_{a,0}, x_{c,0}$	Initial intercalation fractions (anode/cathode)	–
α	Lumped thermal gain from intermediate ROM ($\omega^M \beta$)	$\mathrm{K\,s^{-1}\,C^{-1}}$
β_{ij}	Local heat susceptibility coefficient	$\mathrm{K\,s^{-1}\,A^{-1}}$
γ	Temperature rise per unit charge (final 5pTROM)	$\mathrm{K\,C^{-1}}$
$\Delta\phi_a^{eq}$	Anode OCP	V
$\Delta\phi_c^{eq}$	Cathode OCP	V

Symbol	Description	Units
ε	Surface emissivity	–
σ	Stefan–Boltzmann constant	$\mathrm{W\,m^{-2}\,K^{-4}}$
ρ_{eff}	Effective density of sub-module	$\mathrm{kg\,m^{-3}}$
τ	Internal effective cell-to-matrix relaxation time (intermediate ROM)	s
τ_a	Anode diffusion time constant	s
ω	Matrix thermal diffusion coupling (discrete Laplacian coeff.)	$\mathrm{s^{-1}}$
ω_{ij}	Cell-to-matrix heat transfer rate	$\mathrm{s^{-1}}$
ω_{ij}^{M}	Matrix rate coefficient at (i, j)	$\mathrm{s^{-1}}$
i, j, k	Discrete indices (grid location and sensor index)	–
w_I	Current-channel weight; its value is specified for each objective or metric	–

1. Introduction

The aviation industry is undergoing a fundamental transformation towards Electrified Aircraft Propulsion (EAP), a paradigm shift driven by ambitious goals for sustainability, efficiency, and reduced noise pollution [1]. This transition involves the integration of novel, high-voltage electrical systems—including motors, power electronics, and large-scale battery packs—for which limited operational and service history exists [2]. Among these, the lithium-ion (Li-ion) battery pack imposes key constraints on aircraft design [3, 4], achievable range [4], and operating costs. It also determines safety, reliability, and performance for the viability of an electric flight [5–7]. Battery safety is, in fact, a broader aviation concern: even non-electric aircraft rely on Li-ion energy storage for avionics and emergency systems, where high-profile in-service incidents have underscored the need for rigorous monitoring. Battery-pack health monitoring is also critical for space applications, where sparse sensing and inaccessibility further amplify the importance of model-based diagnostics. Consequently, ensuring the health of these complex energy-storage systems is critical for safety assurance and operational risk management [8]. Advanced Prognostics and Health Management (PHM) systems, capable of providing real-time, actionable information on the battery's internal state, are therefore a foundational enabling technology for the future of aviation [9, 10].

Developing such a PHM system presents a formidable modeling challenge. Battery models can be characterized along two related axes: *physical fidelity*, from empirical to first-principles, and the *model reduction approach* used to obtain the deployed reduced form, from ad hoc construction to systematic reduction from a higher-fidelity physics-based model. Almost every practical workflow ultimately relies on a *reduced-order model* (ROM): a simplified description that retains the behaviors relevant to the targeted decisions. The most widespread ROM family in production battery management systems (BMSs) is the *equivalent-circuit model* (ECM) [11–14], in which voltage dynamics are represented by a small network of resistors and capacitors, with parameters determined by state-of-charge and temperature look-up maps and a separate, loosely coupled lumped thermal surrogate. ECMs are computationally efficient and well matched to real-time deployment. However, because their structure is ad hoc, neither accuracy nor parameter identifiability is guaranteed by construction; both remain empirical properties of each application. Additional sensing modalities—thermal, mechanical, or otherwise—typically require extending the model structure because an ECM explicitly represents only its selected physical couplings. ECM parameters also provide limited access to the electrochemical degradation mechanisms that govern long-term health: a fitted resistance or capacity aggregates the effects of several mechanisms, such as loss of lithium inventory, loss of active material, and interphase growth, which cannot be separated without additional diagnostic tests [15–17].

Physics-based electrochemical models, derived from first principles, sit at the opposite end of the fidelity axis. They describe internal states such as electrode potentials, lithium concentrations, and the growth of parasitic side reactions like the Solid Electrolyte Interphase (SEI) [18–21]. This representation supports prognostics—predicting future performance and remaining useful life—by linking observed behavior to underlying mechanisms and improving extrapolation across operating conditions. However, the practical application of these multiphysics models is hampered by the "curse of dimensionality" in their parameter space [22]. Even a single-particle model contains many parameters (diffusion coefficients, reaction rate constants, activation energies) that are difficult or impossible

to measure non-invasively, especially within an assembled pack [23–25]. This creates a severe identifiability problem: one must infer dozens or hundreds of parameters from the sparse sensor data typically available in operational batteries—namely voltage, current, and a few temperature readings. Most production pack-level workflows sidestep this challenge by collapsing the entire pack to a single equivalent cell—a single set of ECM parameters fitted to pack-level voltage and an averaged temperature. This keeps the parameter count tractable, but it averages over the architecture- and location-dependent variability that is precisely the information needed to localize anomalies to individual bricks, the smallest units resolved by the pack instrumentation. The resulting bottleneck is a critical barrier to deploying next-generation, physics-informed PHM for Li-ion batteries [26, 27].

The natural way to bridge these two extremes is to construct *physics-based, data-driven ROMs*: models whose structure is dictated by the underlying physics, but whose effective parameters are pruned to those that the available sensor data can actually identify. We have pursued this strategy in our prior work, both for single-cell electrochemistry [28] and for single-cell thermal dynamics [29], where a 2-parameter Thermal Reduced-Order Model (2pTROM) was developed and applied to anomaly detection at the cell level [30]. The present work extends this line of investigation from individual cells to a complete, instrumented battery pack.

Even after physics-guided reduction, several parameter combinations can produce nearly indistinguishable voltage and temperature histories and are therefore weakly constrained by the available sensors. Further reduction should follow the distinctions present in the measured predictions. This situation is commonly described as model "sloppiness": the predictions are sensitive to a few parameter combinations and weakly sensitive to many others [31].

The Manifold Boundary Approximation Method (MBAM) provides the conceptual starting point for this task [31–33]. MBAM considers the complete set of predictions obtained as the model parameters vary. At the boundaries of this prediction set, one or more parameters often approach zero or infinity, or combine into a finite product. These limiting relations can expose a simpler model whose predictions remain close to those of the original model. MBAM searches for such boundaries along a *geodesic*: a path that accounts for how local model sensitivities change as the parameters vary. The search is launched in either direction along a weakly constrained, or soft, eigenvector of the Fisher Information Matrix (FIM) $F = J^\top J$, which is the Gauss–Newton approximation to the Hessian of the least-squares cost [31]. The path itself is a geodesic of the FIM-induced metric, and its update requires the directional second derivative of the model outputs, known as the geodesic acceleration. Reported applications of MBAM have concentrated in systems biology and computational physiology [34, 35], with comparatively few in engineering practice [33, 36].

We develop a novel MBAM-inspired procedure, Adaptive Soft-Mode MBAM (AS-MBAM), for practical candidate discovery [37]. AS-MBAM retains the data-driven search for interpretable limiting models and defines the path update by re-evaluating the softest FIM eigendirection at each continuation step. For a model with n parameters, every step therefore reuses the n first-order sensitivity solutions already available from the fit, and the procedure requires no second-order derivative information. For ordinary differential equation models, the geodesic acceleration entails second-order sensitivity equations, automatic-differentiation infrastructure, or repeated perturbed model evaluations or solutions. Quinn *et al.* identify the geodesic calculation as a limitation for larger models [31]. AS-MBAM therefore places systematic candidate discovery within reach of engineering models throughout their development, using the derivative infrastructure that the fitting workflow already maintains. Each interpretable limit found by AS-MBAM is converted into a candidate reduced model, derived analytically, refitted independently, and retained when it remains accurate and sufficiently identifiable. As in MBAM, the path locates candidates and the acceptance test is applied afterwards to the refitted model, which is what makes a first-order path update admissible here. The distinct contribution of AS-MBAM is the recursive, bidirectional, branch-retaining search built on this first-order update and its embedding in the staged reduction of an instrumented engineering system. A closely related first-order update was reported recently for a different application [38].

The present work makes two linked methodological contributions. First, we develop AS-MBAM for generating and testing candidate limiting models. Second, we embed AS-MBAM in a staged reduction chain that connects an HFM with nearly 1300 independent parameters to a physics-based, coarse-grained *thermal* ROM for an instrumented Li-ion pack, in which a few effective parameters per sensor encode the local thermal response while remaining mechanism-linked. The electrochemical sub-model supplies the relation between measured terminal voltage and the local cell current that drives the thermal model. The framework is applied to a 47 kWh Li-ion battery system designed for NASA's X-57 Maxwell electric aircraft [39]. Because the reduction is driven by data-informed identifiability rather than by a prescribed X-57-specific reduced structure, the workflow provides a candidate framework for other Li-ion packs and complex engineered systems in which high-fidelity physics models must be matched to limited sensing.

Application to another system requires re-identification and validation with its own data.

We evaluate the resulting five-parameter Thermal Reduced-Order Model (5pTROM) on one X-57 pack subjected to one laboratory Simulated Flight Profile (SFP) discharge at room temperature (sampling rate 0.5 Hz; 128 series-connected bricks of 20 parallel cells). Under the quasi-adiabatic boundary conditions and loading of this profile, the retained model is consistent with an observable temperature rise that tracks total charge throughput, $\int I\,dt$, more strongly than instantaneous power for the regime probed here [40–43]. Each sensor fit yields four retained quantities (A, $\tilde{r}$, $N_{Li,a}$, and γ) that exhibit coherent pack-wide trends. Because the two fits share the same brick-level voltage and current record, the resulting eight reported quantities are correlated, mechanism-linked diagnostic features with sensor-specific thermal information. Coulomb counting supplies a separate usable-capacity estimate. The present dataset tests common model-form applicability and spatial diagnostic resolution across the pack. Future repeated-mission, aging, and fault-labeled studies will evaluate parameter transfer, anomaly discrimination, and prognostic value.

The paper is organized as follows. Section 2 describes the X-57 battery system and the laboratory dataset. Section 3 establishes the thermal timescales that justify a 2D, quasi-adiabatic sub-module description. Section 4 formulates the coupled thermal–electrochemical HFM of a sub-module and states its identifiability problem. Section 5 develops the physics-guided preliminary reduction, tests it on a toy model, and introduces AS-MBAM together with the resulting toy-model reduction hierarchy. Section 6 applies the reduction to the X-57 data and evaluates the 5pTROM across the pack. Section 7 states the conclusions. The SI gives the mission-segment details, the thermal-property derivations, the AS-MBAM implementation, and the intermediate per-sensor ROMs.

2. System Description

This section provides a description of the X-57 battery system architecture and its nominal loading profile, intended to serve as a foundation for the thermal modeling that follows. Specifications are taken from Ref. [39].

2.1. Battery System Architecture

The X-57 energy storage system is organized as a hierarchy of nested modular units, summarized in Table 1. A *pack* is one 2560-cell, 20P128S assembly of 128 series-connected bricks, and is the unit tested in the laboratory experiment analyzed in Section 6.3. The *battery system* that powers the aircraft consists of two such identical packs wired in parallel for redundancy. Reference [39] calls the pack a "single battery".

This modular and symmetric design is fundamental to the modeling: the thermal environment and boundary conditions of each sub-module are essentially identical, allowing the analysis of a single sub-module to be representative of the entire pack. For thermal management and to prevent thermal runaway propagation, each individual cell is electrically and thermally isolated from its neighbors by a MICA wrap and by a gap-pad disc at its base, which together ensure that a failure in one cell does not propagate to its neighbors.

2.2. Nominal Flight Loading Profile

The experimental evaluation dataset analyzed in this paper consists of a single Simulated Flight Profile (SFP) discharge, performed in a laboratory test on one X-57 battery pack at room ambient temperature, with sensor data sampled at 0.5 Hz. The SFP, defined in Ref. [39], prescribes a sequence of constant-power segments that emulate a complete flight mission, requiring a predicted total energy of 46.2 kW h with a peak power draw of approximately 145 kW. The full mission lasts approximately one hour and proceeds through ground operations (taxi, checklist), takeoff and climb (the most sustained high-power phase, at 25.76 W per cell), cruise, descent and approach, a simulated go-around manoeuvre, final landing and rollout, and a return taxi. A detailed mission-segment description is provided in the Supplementary Information (SI). Model fitting uses the recorded active discharge window shown in Fig. 2; the low-power taxi segments lie outside this recorded evaluation window. This loading schedule provides a realistic nominal test of the fitted model form. Future repeated-profile studies will provide cross-profile predictive validation.

Table 1: X-57 Maxwell battery system architecture and instrumentation, with counts given per parent unit and per battery system. Specifications from Ref. [39].

Level	Per parent	Per system	Specification
Battery system	—	1	386 kg (850 lb); 47 kW h; 5120 cells
Pack	2 (parallel)	2	20P128S; 2560 cells; 461 V nominal (320 V to 538 V); 60 A h
Module	8	16	20P16S; 320 cells
Sub-module	2	32	20P8S; 160 cells in a 16×10 aluminum honeycomb scaffolding (Fig. 1)
Brick	8 (series)	256	20P1S; 20 parallel cells; the basic identifiable unit for health monitoring
Cell	20 (parallel)	5120	Samsung INR18650-30Q cylindrical Li-ion; 3.60 V, 3.0 A h nominal
Instrumentation			
Thermocouple	16 per sub-module	512	Attached to the aluminum honeycomb at *ad hoc* locations, two per brick
Voltmeter	8 per sub-module	256	One across each series-connected brick
Ammeter	1 per pack	2	The 128 bricks of a pack form one series chain, so a single current record applies to every brick and sub-module of that pack

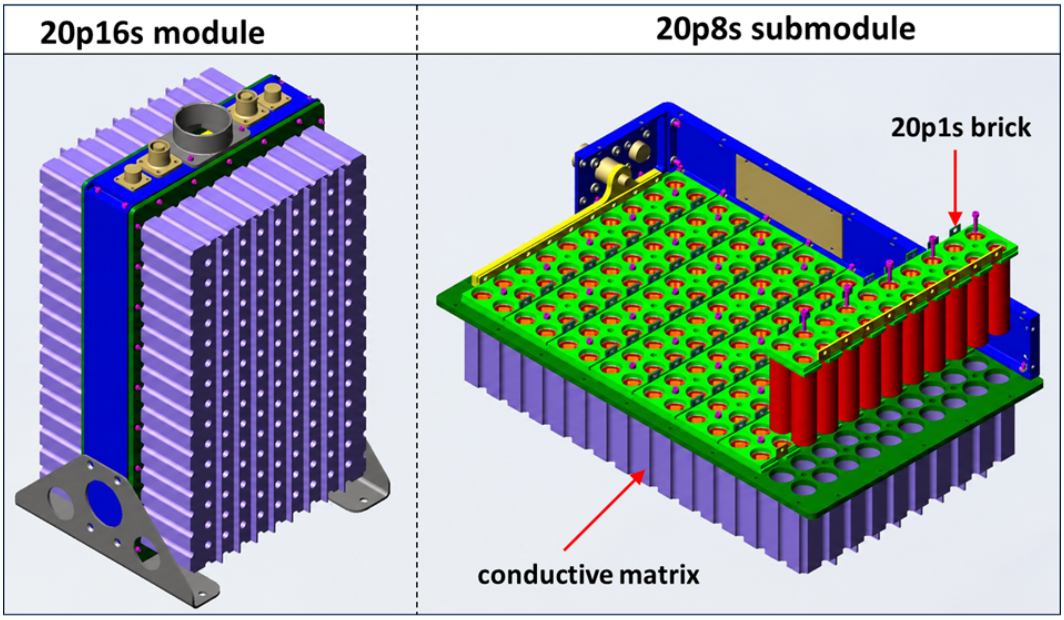


Figure 1: Architecture of an X-57 module and sub-module (CAD renderings reproduced from Ref. [39]). *Left:* the 20P16S module. *Right:* the 20P8S sub-module, with one "20P1S brick" (20 parallel cells in series with the rest of the bricks) labeled at the top right and the surrounding aluminum conductive matrix labeled at the bottom left. The conductive matrix is the honeycomb scaffolding in which the cylindrical cells are housed; it provides both mechanical support and the dominant in-plane thermal-conduction pathway exploited by the thermal model in Section 4.1.

3. Thermal Relaxation Timescale Analysis

To justify the modeling choice adopted in the next section, we briefly summarize the result of an order-of-magnitude analysis of the dominant heat-transfer mechanisms in a single sub-module; the full derivation, including the effective thermal properties of the composite and the calculation of the relevant timescales, is provided in the SI.

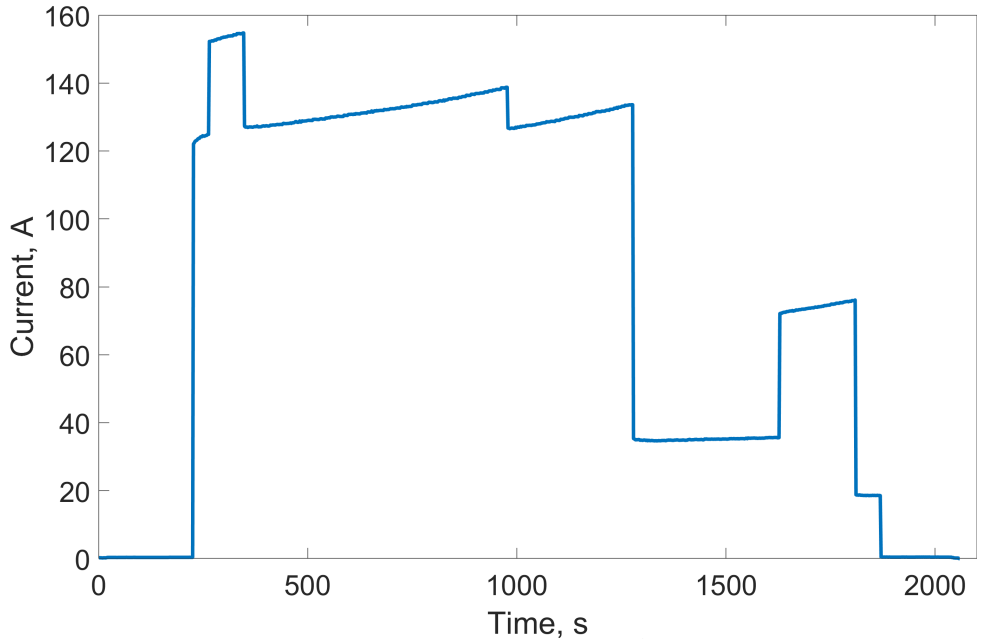


Figure 2: Brick-level current measured during the laboratory Simulated Flight Profile (SFP) discharge window analyzed in this paper. The trace shows the high-power takeoff/climb phase, an extended cruise plateau, the lower-power descent and approach, the go-around segment, and the final low-power recorded segment. The full SFP mission definition also includes low-power taxi segments described in the SI; these segments lie outside the recorded evaluation window. This SFP discharge of a single X-57 pack at room ambient temperature, sampled at 0.5 Hz, constitutes the experimental evaluation dataset used in Section 6.3.

We treat the sub-module as a homogeneous block with effective anisotropic properties: volume fractions estimated from the CAD images in Ref. [39] give through-thickness and in-plane conductivities $k_{\perp} \approx 64\,\mathrm{W\,m^{-1}\,K^{-1}}$ and $k_{\parallel} \approx 42\,\mathrm{W\,m^{-1}\,K^{-1}}$ (Section S2.3 of the SI). External heat loss combines natural convection ($h_{\mathrm{conv}} \approx 5\,\mathrm{W\,m^{-2}\,K^{-1}}$) and thermal radiation ($h_{\mathrm{rad}} \approx 5\,\mathrm{W\,m^{-2}\,K^{-1}}$) into an effective coefficient $h_{\mathrm{total}} \approx 10\,\mathrm{W\,m^{-2}\,K^{-1}}$ at a representative laboratory ambient of 20 °C. The radiation coefficient $h_{\mathrm{rad}} = \varepsilon\sigma(T_{\mathrm{hot}}^2 + T_{\mathrm{cold}}^2)(T_{\mathrm{hot}} + T_{\mathrm{cold}})$ reproduces the Stefan–Boltzmann flux $\varepsilon\sigma(T_{\mathrm{hot}}^4 - T_{\mathrm{cold}}^4)$ exactly; treating it as constant is the only approximation, and it varies from 4.6 to $5.3\,\mathrm{W\,m^{-2}\,K^{-1}}$ between 21 and 50 °C, well inside the factor-of-two range over which the conclusions below are tested in the SI. The SI analysis yields two key results. First, the Biot number across the sub-module thickness is $Bi \approx 0.016 \ll 0.1$, so internal thermal resistance through the thickness is negligible and a 2D in-plane treatment is justified. Second, the characteristic external cooling time is approximately 6.7 h, much longer than the ~ 1 h SFP discharge analyzed here. Together, these two results justify modeling the sub-module as a 2D, quasi-adiabatic system over the duration of a single SFP test, with zero-flux (adiabatic) boundary conditions on all sub-module faces.

The 20 °C ambient used in the timescale estimate corresponds to the laboratory evaluation test. Flight-specific ambient temperature, airflow, and ventilation would require re-evaluation of the effective heat-transfer coefficients, the quasi-adiabatic approximation, and the calibrated parameters.

4. The sub-module Model

4.1. Coupled Cell-Matrix Thermal Model

Based on the physical architecture and the timescale analysis, a discretized thermal model for a single sub-module is developed, Figure 3. The sub-module is represented as a grid of $N_1 \times N_2$ cells (where $N_1 = 10$, $N_2 = 16$) immersed in the aluminum matrix. The matrix itself is subdivided into a corresponding grid of $N_1 \times N_2$ sub-volumes, with each

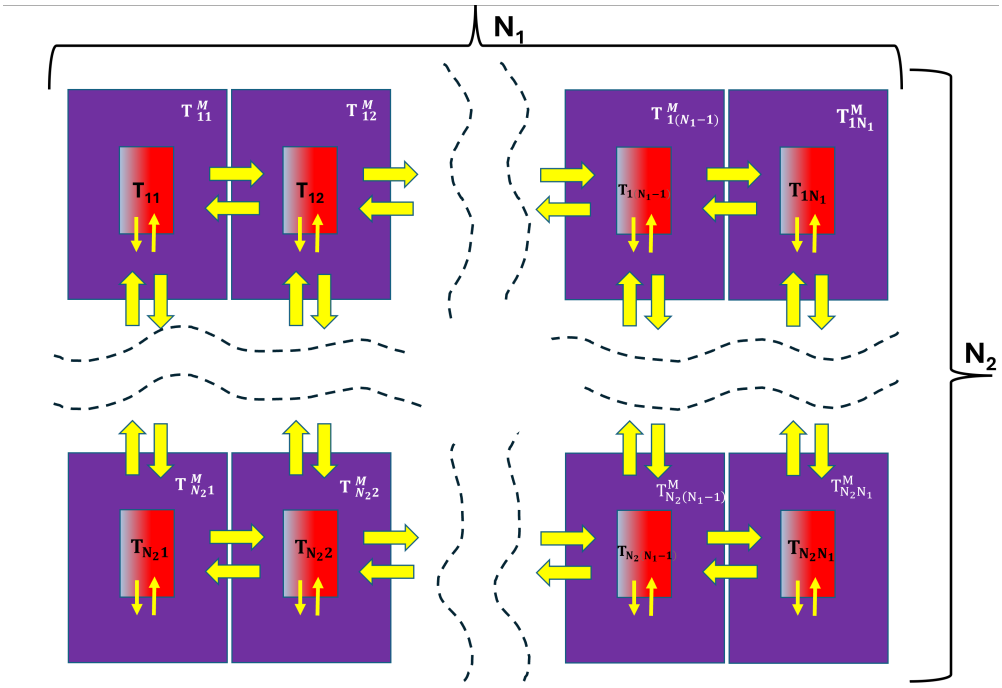


Figure 3: Schematic of the discretized, coupled thermal model for a single X-57 sub-module. The sub-module is represented as an $N_1 \times N_2$ grid. Each cell, with temperature T_{ij}, is thermally coupled to a corresponding sub-volume of the surrounding aluminum honeycomb matrix, which has temperature T_{ij}^M. The yellow arrows depict the modeled heat transfer pathways: (1) exchange between each cell and its local matrix sub-volume, and (2) conduction between adjacent matrix sub-volumes.

cell thermally coupled to its local sub-volume. The model tracks the temperature of each cell, denoted by T_{ij}, and the temperature of the corresponding matrix sub-volume, T_{ij}^M.

The model for the thermal dynamics of an individual cell is adapted from our previous work [29], where a 2-parameter Thermal Reduced-Order Model (2pTROM) was developed to describe local heat generation and dissipation in a cell. Although that work involved a different loading profile, a subsequent study [30] confirmed that the 2pTROM remains an adequate model to describe the thermal behavior of a single cell under X-57 loading conditions. Consequently, the 2pTROM was adopted as a validated building block for modeling the heat generation term for each cell within the full sub-module.

The governing equations for the temperature evolution of the cells and the matrix sub-volumes are given by the following system of coupled differential equations:

$$\frac{dT_{ij}}{dt} = \beta_{ij} I_{ij}(t) - \omega_{ij}\left(T_{ij} - T_{ij}^M\right), \quad i = 1,\ldots,N_1, \quad j = 1,\ldots,N_2, \tag{1}$$

$$\begin{aligned}\frac{dT_{ij}^M}{dt} &= \omega_{ij}^M\left(T_{ij} - T_{ij}^M\right) + \omega\left(T_{i+1,j}^M - 2T_{ij}^M + T_{i-1,j}^M\right) \\ &\quad + \omega\left(T_{i,j+1}^M - 2T_{ij}^M + T_{i,j-1}^M\right).\end{aligned} \tag{2}$$

These equations describe the flow of heat through the sub-module. Equation (1) models the temperature of an individual cell. The cell's temperature rises due to heat generation, represented by $\beta_{ij} I_{ij}(t)$, where β_{ij} is the local heat susceptibility and $I_{ij}(t)$ is the current, according to the 2pTROM. This formulation allows for cell-to-cell variations in heat generation, which is critical for representing real-world conditions [29]. The cell's temperature decreases as it transfers heat to the local matrix, a process governed by the cell-to-matrix heat transfer rate ω_{ij}. Each cell–matrix pair has the structure of the two-state lumped models used to estimate the core temperature of a cylindrical cell from a sensor on its casing [40, 44]; here the second state is the matrix sub-volume, and the thermocouple is attached to the matrix.

Equation (2) models the temperature of the corresponding matrix sub-volume. The term $\omega_{ij}^{M}\left(T_{ij}-T_{ij}^{M}\right)$ is the direct counterpart to the heat loss from the cell, representing the heat absorbed by the matrix sub-volume. The coefficient ω_{ij}^{M} governs the rate of temperature increase in the matrix resulting from this heat transfer. The matrix sub-volume then exchanges this heat with its four nearest neighbors via conduction, as described by the final two terms, which represent a finite difference approximation of the 2D thermal diffusion operator ($\nabla^2 T$). The constant ω represents the thermal coupling within the conductive honeycomb matrix. This model operates under the adiabatic boundary conditions justified in Section 3, making it a self-contained representation of the sub-module's thermal dynamics over the laboratory SFP discharge. Flight conditions (ambient temperature, airflow, ventilation) require re-evaluating the external heat-transfer coefficients and the quasi-adiabatic approximation.

4.2. Local Current Electrochemical Model

The thermal model described in Section 4.1 requires the local cell current, $I_{ij}(t)$, as an input for the heat generation term. To determine these currents, we adopt a reduced-order electrochemical model (ROM) for a single Li-ion cell, derived from a Single-Particle Model in our prior work [28]. The model relates the cell's terminal voltage, $V(t)$, to its current and internal states:

$$V(t) = \Delta\phi_c^{eq}(\bar{x}_c(t)) - \Delta\phi_a^{eq}(\bar{x}_a(t)) - I(t)\cdot\tilde{r}, \tag{3}$$

where $\Delta\phi_c^{eq}$ and $\Delta\phi_a^{eq}$ are the open-circuit potentials (OCPs) of the cathode and anode, respectively, and $\tilde{r}$ is an effective series resistance. The variables $\bar{x}_a(t)$ and $\bar{x}_c(t)$ represent the lithium intercalation fractions at the surface of the anode and cathode: $\bar{x}_a \equiv x_a/x_{a,0}$ and $\bar{x}_c \equiv (1-x_c)/(1-x_{c,0})$, where $x_{a,0}$ and $x_{c,0}$ are the initial intercalation fractions in the anode and cathode of a fully charged cell.

In an operational setting, the OCPs are inferred indirectly from the voltage, current, and thermal data. The foundational OCP model proposed by Verbrugge and coworkers [19] and elaborated by Birkl *et al.* [20]—which we refer to in what follows as the Verbrugge–Birkl ansatz—captures the OCP dependence on the intercalation fraction in detail but involves dozens of parameters. Given the indirect nature of the present measurements, it is highly probable that most of these parameters would be non-identifiable, necessitating a model reduction procedure. Anticipating this, we adopt from the outset a simplified parameterization of the Verbrugge–Birkl ansatz, which can be viewed as a hypothesis for what a reduced-order version of the OCV model might look like. Two qualitative features of the underlying physics guide this reduced parameterization:

- *Cathode.* Within the operational state-of-charge (SOC) window relevant to the SFP discharge, the cathode OCP is smooth and bounded; the Verbrugge–Birkl curve is approximately monotone with a finite slope. To leading order, this is well captured by a linear function $\Delta\phi_c^{eq}(\bar{x}_c) = A_c + B_c\bar{x}_c$ over the relevant SOC range.
- *Anode.* The Verbrugge–Birkl anode OCP exhibits a characteristic logarithmic-type divergence as the surface intercalation fraction approaches zero, which dominates the cell voltage near full discharge. The simplest functional form that retains this divergence while remaining smooth at higher intercalation is $\Delta\phi_a^{eq}(\bar{x}_a) = A_a - B_a\log\bar{x}_a$.

These two ansatzes preserve the qualitative shapes of the cathode and anode OCPs that are most consequential for the voltage–current relation under the SFP load, while reducing the number of OCP parameters from many to four (A_c, B_c, A_a, B_a). The validity of this simplified model is ultimately justified by its performance against experimental data; should it prove inadequate, the parameterization could be reconsidered. Substituting the resulting OCP forms into Eq. (3) yields the following equation for the terminal voltage:

$$V(t) = A + B_c\bar{x}_c(t) + B_a\log\bar{x}_a(t) - I(t)\cdot\tilde{r} \tag{4}$$

Here, the constants from the ansatz are lumped into three parameters: $A = A_c - A_a$, B_c and B_a. The internal states $\bar{x}_c(t)$ and $\bar{x}_a(t)$ depend on the history of the current, governed by solid-phase diffusion dynamics [28]:

$$\bar{x}_c(t) = 1 - \int_0^t \frac{I(t')dt'}{eN_{Li,c}}, \tag{5}$$

$$\bar{x}_a(t) = 1 - \frac{1}{3eN_{Li,a}}\int_0^t h\left(\frac{t'}{\tau_a}\right) I(t-t')dt', \tag{6}$$

where $N_{Li,a}$ is the total number of Li ions available for intercalation into the anode, $N_{Li,c}$ is the total number of intercalation sites in the cathode, τ_a is the anode's diffusion time constant, and $h(t')$ is the inverse Laplace transform of the diffusion transfer function, $h(t') = \mathcal{L}^{-1}\left[(\sqrt{\zeta}\coth\sqrt{\zeta}-1)^{-1}\right](t')$. Only the anode diffusion is retained: the cathode diffusion dynamics were eliminated in the systematic reduction of the single-particle model in Ref. [28]. In the present data the anode diffusion is eliminated in turn (Section 6), so the final model contains no solid-phase diffusion dynamics. This formulation results in a model governed by six parameters: A, B_a, τ_a, $N_{Li,a}$, $N_{Li,c}$ and $\tilde{r}$. The seventh parameter B_c is constrained by the initial fully-charged voltage, $A+B_c = V(0)$. These six parameters are not independent: the following reparameterization reduces their number by one: $A'+B'_c = A+B_c$ and $B_cN_{Li,a} = B'_cN_{Li,c}$, leading to

$$V(t) = A' + B'_c\bar{x}'_c(t) + B_a\log\bar{x}_a(t) - I(t)\cdot\tilde{r}, \tag{7}$$

$$\bar{x}'_c(t) = 1 - \int_0^t \frac{I(t')dt'}{eN_{Li,a}}, \tag{8}$$

$$\bar{x}_a(t) = 1 - \frac{1}{3eN_{Li,a}}\int_0^t h\left(\frac{t'}{\tau_a}\right)I(t-t')dt', \tag{9}$$

governed by just five independent parameters: A', B_a, τ_a, $N_{Li,a}$ and $\tilde{r}$ (the sixth parameter B'_c is fixed by $A'+B'_c = V(0)$). For brevity, we henceforth drop primes and write A and $\bar{x}_c(t)$ in place of A' and $\bar{x}'_c(t)$.

For our purposes, we invert this model to determine the current $I(t)$ from a given voltage profile $V(t)$. By rearranging Eq. (7) and substituting the expression for $I(t)$ into the equations for $\bar{x}_a(t)$ and $\bar{x}_c(t)$, we obtain a closed system of integro-differential equations:

$$I(t) = \frac{A + B_c\bar{x}_c(t) + B_a\log\bar{x}_a(t) - V(t)}{\tilde{r}}, \tag{10}$$

$$\bar{x}_c(t) = 1 - \frac{1}{eN_{Li,a}}\int_0^t I(t')dt', \tag{11}$$

$$\bar{x}_a(t) = 1 - \frac{1}{3eN_{Li,a}}\int_0^t h\left(\frac{t-t'}{\tau_a}\right)I(t')dt'. \tag{12}$$

This system is applied to each cell in the sub-module. The five independent parameters (A, B_a, τ_a, $N_{Li,a}$, and $\tilde{r}$) capture local properties of each cell ($_{ij}$), allowing for cell-to-cell variability. The input voltage $V(t)$ is assumed to be uniform and given for all cells within the same parallel-connected brick of the sub-module.

4.3. The Challenge of Model Identifiability

The High-Fidelity Model (HFM) detailed in Sections 4.1 and 4.2 contains nearly 1300 independent parameters—481 thermal (three per cell for 160 cells, plus the global matrix coupling ω) and 800 electrochemical (the five independent per-cell parameters of Section 4.2 for each of the 160 cells)—while each sub-module is observed through 25 measurement streams: 16 thermocouples, 8 voltmeters, and a single ammeter. Each stream contains many time samples, so parameter identifiability is governed by the distinguishability of parameter combinations in the measured outputs. Sparse spatial sensing, structural parameter symmetries, and strongly anisotropic sensitivities make many parameter combinations weakly observable. In the information-geometric language of Quinn *et al.*, the HFM is therefore a sloppy multiparameter model [31]. The explicit scaling degeneracy derived later and the toy-model fits illustrate these mechanisms. Systematic reduction constructs a model whose retained parameters are supported by the available observations.

5. Model Reduction

5.1. First step: Physics-Guided Preliminary Reduction

The analysis in Section 4.3 shows that the HFM contains substantially more parameter detail than the available sensing resolves, motivating simplification. A common strategy for reducing such "sloppy" models involves taking certain parameters to their physical limits (e.g., zero or infinity) in a way that remains consistent with the experimental

data [28, 29, 31]. While this can be done through systematic computational methods [32, 33], a *physics-guided preliminary reduction*—in which structural simplifications are made on the basis of physical scaling principles before any data-driven reduction is invoked—is often highly effective for an initial, significant reduction [28, 29]. We adopt such a physics-guided preliminary reduction as the first step in our model reduction.

Our reduction is based on the conjecture, supported by the general principles of model identification [45, 46], that the number of identifiable parameters in a viable ROM should scale with the number of sensors, L. For our thermal model, $L = 16$ is the number of thermocouples per sub-module (two per brick), and the local cell currents are treated as known inputs. We seek a reduction path that achieves this scaling. Looking at the governing equations, an immediate path to achieve this is to take the cell-to-matrix coupling coefficients ω_{ij}^M to their limit of zero for all cells not located at a thermocouple position (i_k, j_k), $k = 1, 2, ..., L$. This simplification prunes the HFM significantly, resulting in a ROM where only the L cells actively heat the matrix in the vicinity of the L thermocouple locations.

The governing equations for this ROM are then given as follows. For the L cells and matrix sub-volumes at thermocouple locations ($k = 1, ..., L$):

$$\frac{dT_{i_k,j_k}}{dt} = \beta_{i_k,j_k} I_{i_k,j_k}(t) - \omega_{i_k,j_k}\left(T_{i_k,j_k} - T^M_{i_k,j_k}\right), \tag{13}$$

$$\begin{aligned}\frac{dT^M_{i_k,j_k}}{dt} &= \omega^M_{i_k,j_k}\left(T_{i_k,j_k} - T^M_{i_k,j_k}\right) + \omega\left(T^M_{i_k+1,j_k} - 2T^M_{i_k,j_k} + T^M_{i_k-1,j_k}\right) \\ &\quad + \omega\left(T^M_{i_k,j_k+1} - 2T^M_{i_k,j_k} + T^M_{i_k,j_k-1}\right),\end{aligned} \tag{14}$$

and for all other matrix sub-volumes at locations (i, j) not corresponding to a thermocouple:

$$\frac{dT^M_{ij}}{dt} = \omega\left(T^M_{i+1,j} - 2T^M_{ij} + T^M_{i-1,j}\right) + \omega\left(T^M_{i,j+1} - 2T^M_{ij} + T^M_{i,j-1}\right). \tag{15}$$

This ROM, which we termed (3L+1)pTROM, is governed by $3L + 1 = 49$ parameters: three parameters (β_{i_k,j_k}, ω_{i_k,j_k}, $\omega^M_{i_k,j_k}$) for each of the $L = 16$ measured locations, plus the single global matrix diffusion constant ω. This simplification can be understood through the concept of *parameter renormalization*, a technique common in the study of complex systems [31]. Suppressing the explicit heat-source terms for the $160 - 16 = 144$ unmeasured matrix subvolumes assigns their collective slow-timescale influence on the measured locations to the effective local parameters (β_{i_k,j_k}, ω_{i_k,j_k}, $\omega^M_{i_k,j_k}$). The ROM is therefore an *effective theory* for the sensor locations, with coarse-grained parameters that integrate the influence of the wider system. The toy-model experiment below tests the accuracy of this effective description over the observed window.

The (3L+1)pTROM admits an effective separation-of-timescales interpretation. Heat transfer from the $L = 16$ cells adjacent to thermocouples forms the fast, sensor-resolved contribution, while the collective influence of the remaining 144 cells is absorbed into the effective local parameters over the flight-duration window. This data-consistent description represents the timescale decomposition at the resolution provided by the available observations.

We evaluate the physics-guided reduction in two stages. First, a simplified toy model with synthetic data tests the hypothesis of effective local thermal dominance for selected system sizes, sensor locations, and inputs. The resulting sensor-scaled ROM then serves as the starting point for further reduction, and the final common local structure is evaluated against the experimental X-57 data. Broader tests will extend this assessment across additional architectures and loading profiles.

5.2. Testing the Reduction Hypothesis with a Toy Model

To test the model reduction hypothesis in a controlled setting, we employ a toy model. For computational simplicity, we use a simple but nontrivial system: a linear string of $N = 6$ cells immersed in a conductive matrix, with measurements assumed at two generic sites, $i_1 = 2$ and $i_2 = 5$ [1]. The governing equations for this toy system are derived from the general equations for the HFM, Eqs. (1)–(2), and the (3L+1)pTROM, Eqs. (13)–(15), for $N_1 = 6, N_2 = 1$. The

[1] A system of size $N = 5$ is the mathematical minimum required to place two sensors (e.g., at positions 2 and 4) such that they are non-adjacent and neither is at a boundary. The choice of $N = 6$ in this work, with sensors at positions $i_1 = 2$ and $i_2 = 5$, satisfies these conditions while also creating a more generic, asymmetric test case with two unmeasured cells between the sensors rather than one.

HFM thus has 19 parameters (three per cell—β_i, ω_i, ω_i^M—for $N = 6$ cells, plus the single matrix diffusion constant ω), while its physics-guided reduction to the (3L+1)pTROM has $3L + 1 = 7$ parameters (three per measured cell at i_1 and i_2, plus ω). The toy model is purely thermal: each of the six cells receives its own prescribed current, and no electrical connection between cells is modeled. For the input, we use independent "random walk" current profiles, piecewise-constant levels drawn at random over fixed intervals and followed by a zero-current relaxation period, similar to loading seen in small UAV applications [30]; Fig. 4(a) shows the profiles of the two measured cells. Prescribing the currents directly, rather than inferring them from voltage through the electrochemical model, isolates the thermal reduction problem from electrochemical-parameter identifiability, providing a controlled test of the thermal reduction hypothesis.

The test follows a "simulate-and-fit" procedure where the 7-parameter (3L+1)pTROM is fit to synthetic data generated by the 19-parameter HFM. To ensure a robust exploration of the parameter space and to avoid convergence to local minima, a multi-start optimization is performed. The fit uses the Nelder–Mead simplex algorithm (MATLAB `fminsearch`) and is repeated 1500 times, each run starting from initial parameters drawn independently and uniformly within $\pm 90\%$ of the HFM values at the measured cells. Each point in the parameter-error plots of Fig. 4(c-f) represents the final converged result—the fitted parameters and their corresponding RMSE—of one such optimization trial. Unless otherwise specified, reported RMSE values in this paper are normalized and dimensionless. For a fit over one or more reported channels, the mean square error (MSE) of each channel is normalized by the mean-square value of that channel's measured signal, taken relative to its initial value, over the observed window; when multiple channels are included in the reported RMSE, the RMSE is the square root of the sum of those normalized MSE contributions. Thus the RMSE is interpretable as an aggregate relative error on the stated output channels. The collective results of these trials show two key findings. First, the (3L+1)pTROM is accurate; both predicted matrix temperatures $T_{i_1}^M$, $T_{i_2}^M$ are visually very close to the ground-truth data (Fig. 4(b)). Second, the model exhibits practical non-identifiability. The parameter-error plots (Fig. 4(c-f)) show that a wide range of parameter sets yield good fits—RMSE < 0.025—a classic signature of a "sloppy" model. This dual finding of accuracy and non-identifiability was robustly observed across other tested configurations, including systems with up to 20 cells and varied sensor locations.

This result—accuracy coupled with practical non-identifiability—is a critical intermediate finding. It supports the initial reduction hypothesis while demonstrating the necessity for a second reduction step. The subsequent sections therefore focus on the systematic derivation of a lower-dimensional ROM with improved practical identifiability for the present diagnostic application and on its pack-wide evaluation against the available experimental X-57 data.

5.3. Adaptive Soft-Mode MBAM: Recursive Branching Candidate Search

The toy-model fit reproduces both temperature records accurately while leaving broad parameter combinations weakly constrained: widely different parameter sets produce nearly the same predictions. The remaining reduction problem is to identify these soft parameter combinations and determine whether their limiting behavior yields a simpler model.

This subsection defines AS-MBAM for a general least-squares model; the toy model of Section 5.2 serves as the running instance, and the X-57 specialization follows in Section 6.2. MBAM inspired this strategy by associating simple reduced models with boundaries—limiting cases—of the set of possible model predictions [31–33]. We developed AS-MBAM to search for such limits using the first-order sensitivities already available from model fitting. For the toy model, these sensitivities quantify the immediate change of the two sensor-temperature histories under a parameter perturbation. The same sensitivity infrastructure therefore supports fitting, identifiability analysis, and candidate discovery. Interpretable limiting relations are converted into reduced-model candidates and evaluated by analytical derivation, independent refitting, accuracy, and identifiability.

Let c index a fitted output *channel*, meaning the temperature history associated with one sensor location, and let n index a *sample*, meaning one time point in that history. For the toy model introduced above, the channels are the two predicted matrix-temperature traces $T_{i_1}^M$ and $T_{i_2}^M$. For physical parameters p, we define the normalized residual components and their least-squares cost by

$$r_{c,n}^{\mathrm{AS}}(p) = \sqrt{w_c}\,\frac{y_{c,n}^{\mathrm{model}}(p) - y_{c,n}^{\mathrm{data}}}{S_c}, \qquad C_{\mathrm{AS}}(p) = \frac{1}{2}\sum_c \sum_n \left[r_{c,n}^{\mathrm{AS}}(p)\right]^2. \tag{16}$$

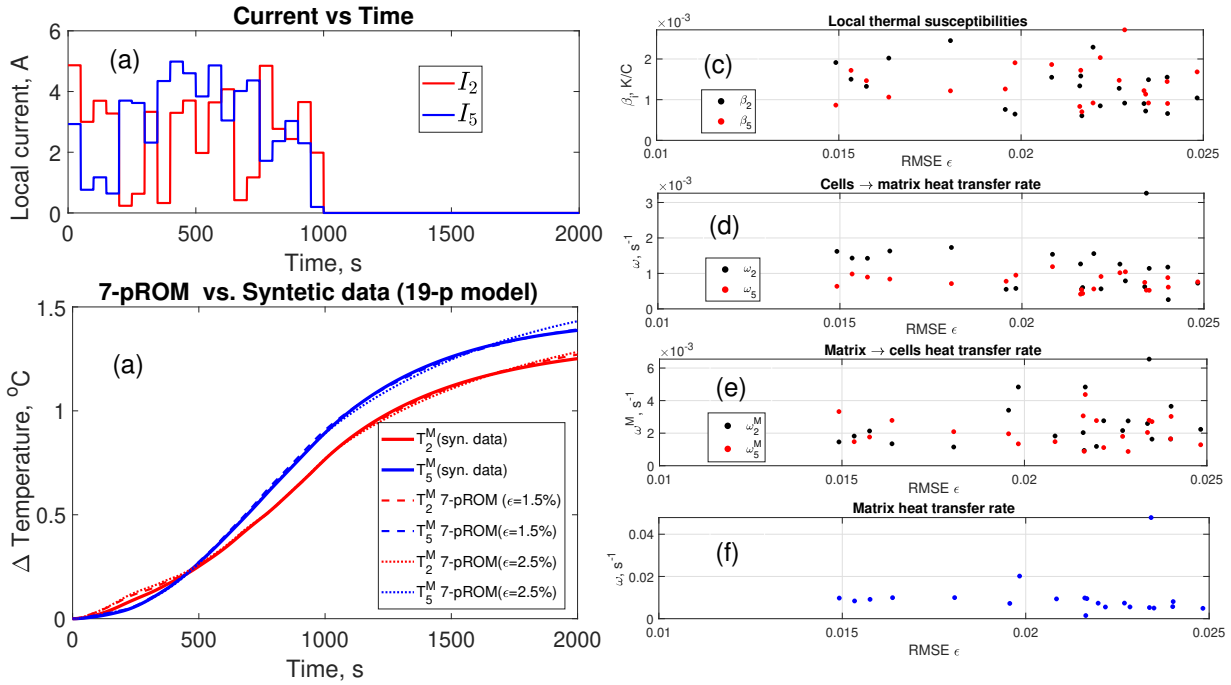


Figure 4: Results of the toy-model numerical experiment, with sensors located at $i_1 = 2$ and $i_2 = 5$. **(a)** The "random walk" input current profiles of the two measured cells; each of the six cells receives an independent profile. **(b)** The fitted 7-parameter (3L+1)pTROM demonstrates high predictive accuracy: the predicted matrix temperatures $T_{i_1}^M$ and $T_{i_2}^M$ (dashed lines for total RMSE $\varepsilon = 0.015$, dotted lines for $\varepsilon = 0.025$) closely track the corresponding "ground-truth" matrix-temperature traces (solid lines) generated by the 19-parameter HFM. **(c–f)** Final fitted parameter values versus the total root-mean-square error (RMSE, ε). Each point shown is the final converged result of an individual optimization trial from a multi-start procedure, which robustly explores the parameter space by running the fit from 1500 random starting points. The total RMSE is computed from the individual mean-squared errors of the two matrix-temperature traces, $\text{RMSE} = \sqrt{\text{MSE}_1 + \text{MSE}_2}$, where each MSE_i is the mean-squared deviation of the predicted trace T_i^M from the data, normalized by the mean-square value of T_i^M over the observed window. Both MSE_i and RMSE are therefore dimensionless and represent errors relative to the root-mean-square signal. Note that the average RMSE per individual matrix-temperature series is therefore smaller by a factor of approximately $\sqrt{2}$. The wide distributions for low-error fits are a classic signature of practical non-identifiability.

Here $y_{c,n}$ denotes the predicted or measured temperature at sensor channel c and time t_n. For the present toy model,

$$y_{1,n} = T_{i_1}^M(t_n), \qquad y_{2,n} = T_{i_2}^M(t_n).$$

The quantity S_c is the root-mean-square value of the measured channel c over the observed window and w_c is its weight. The toy-model reduction uses the two temperature channels with equal weights, consistent with the total-error definition in Fig. 4. Other applications can use different channel sets and normalizations; the X-57 specialization is stated in Section 6.2 and detailed in Section S3.5 of the SI.

The physical-parameter Jacobian is $J_p = \partial r^{\text{AS}}/\partial p$. The continuation is computed in dimensionless relative coordinates

$$q_i = \frac{p_i}{p_{0,i}}, \qquad p = \left[\beta_{i_1}, \omega_{i_1}, \omega_{i_1}^M, \beta_{i_2}, \omega_{i_2}, \omega_{i_2}^M, \omega\right]^\top \quad \text{for the initial toy-model ROM,} \tag{17}$$

where p_0 is the local best-fit parameter vector. Subsequent toy-model ROMs use the corresponding retained parameter vector in the same relative-coordinate construction. The Jacobian and the least-squares/Gauss–Newton Fisher Information Matrix (FIM), used here as a local sensitivity metric [31], are

$$J_q = J_p \,\text{diag}(p_0), \qquad F_q = J_q^\top J_q. \tag{18}$$

F_q is the Gauss–Newton approximation to the Hessian of C_{AS}, exact in the zero-residual limit and accurate near a good fit, where the residual-weighted second-derivative term is small; Section S3.1 of the SI gives the exact relation.

Large eigenvalues of F_q identify stiff directions that strongly change the normalized residuals. Small eigenvalues identify soft directions. At a stationary best fit $q_0 = \mathbf{1}$, a displacement of magnitude δ along a unit eigenvector v with eigenvalue λ gives the Gauss–Newton cost increase

$$C_{\mathrm{AS}}(q_0 + \delta v) - C_{\mathrm{AS}}(q_0) \simeq \frac{1}{2}\lambda\delta^2. \tag{19}$$

The smallest-eigenvalue eigenvector $v^{(q)}_{\mathrm{min}}$ is therefore the locally least costly quadratic direction at the best fit. Away from the best fit, it is the unit direction that produces the smallest first-order change in the selected normalized residual vector. The continuation is therefore defined by a sequence of locally soft directions, with the global path generated by repeated local updates. The resulting path is therefore not a geodesic of the FIM-induced metric; the two updates are compared below and in Section S3.2 of the SI.

AS-MBAM re-evaluates the softest direction along the continuation and evolves

$$\frac{dq}{ds} = \frac{v^{(q)}_{\mathrm{min}}(q)}{\left\| v^{(q)}_{\mathrm{min}}(q) \right\|}, \tag{20}$$

where s is a dimensionless continuation parameter or pseudo-time and $\|\cdot\|$ denotes the Euclidean length. Dividing by this length makes the right-hand side a unit direction. Relative coordinates prevent parameters with large numerical magnitudes or different units from dominating that length solely because of their scale.

An eigenvector defines an axis with two opposite orientations. We therefore integrate Eq. (20) from the best fit with initial directions $+v^{(q)}_{\mathrm{min}}$ and $-v^{(q)}_{\mathrm{min}}$, since the two branches can approach different parameter limits. This bidirectional launch is also used in standard MBAM [31]. The soft direction is recomputed at every step of the continuation; Section S3.2 of the SI compares this update with the geodesic update.

Equation (20) admits a simple interpretation: the continuation follows the locally softest direction of the normalized error landscape, sketched in Fig. 5. It is stated entirely in terms of objects that an identifiability analysis already produces—a least-squares Jacobian and an eigendecomposition of F_q—so implementing the search requires no apparatus beyond what the fitting workflow provides. Two consequences of this construction should be stated explicitly. First, the softest eigenvector, and hence the path, depends on the coordinates in which F_q is expressed; a geodesic of the FIM-induced metric is coordinate independent. We therefore fix the coordinates explicitly as the relative parameters of Eq. (17), which makes the scaling a declared modeling input. Second, the continuation serves as a candidate generator. In MBAM and in AS-MBAM alike, a limit reached by the path is identified by inspection, derived analytically, and refitted independently before acceptance, and accuracy and identifiability are assessed on the refitted model. Path construction therefore determines only which candidates the search encounters; acceptance is decided on the refitted model, which makes a first-order update admissible. What the path construction does affect is the likelihood of reaching an interpretable limit before the error leaves the adopted acceptance range, as happened on the terminated branch of Section 6.2.

For each branch, we inspect the parameter combinations and fit-error diagnostic until the trajectory approaches an interpretable limit or leaves the adopted acceptance range. The limiting model is then derived analytically and refitted independently. Accepted candidates seed the next reduction level or proceed to application-level evaluation, producing the branching tree used below.

5.4. Systematic Reduction Hierarchy of the Toy Model

The 7-parameter toy-model (3L+1)pTROM, termed `M0` for brevity, was reduced using AS-MBAM. The present search produced a branching hierarchy of simpler models, summarized in Table 2 and visualized in the SI. The search terminates in a set of branch-terminal candidates under the adopted error criterion. The retained set includes three 4-parameter models—`M0-dir1-dir1-dir2` (RMSE=0.032), `M0-dir1-dir2-dir2` (RMSE=0.033), and `M0-dir2-dir2-dir1` (RMSE=0.023)—and one 3-parameter model, `M0-dir2-dir2-dir2-dir1` (RMSE=0.028).

The coexistence of several branch-terminal ROMs with comparable errors is itself a reduction result: the same forcing and measured outputs support multiple effective descriptions with different retained mechanisms. By exposing alternative low-error boundary models, the recursive tree probes the uniqueness of the reduced explanation. The

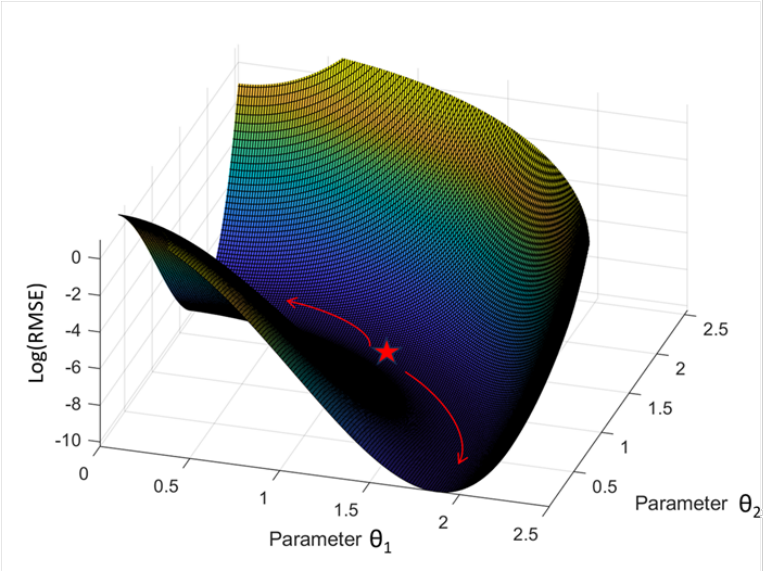


Figure 5: Schematic of a local error landscape near a best-fit point (red star). The stiff direction produces a large local residual change, whereas the soft direction produces a small one. The arrows show the two initial orientations of the smallest-eigenvalue direction from which AS-MBAM generates candidate continuations. The continuation of Eq. (20) follows the soft direction, re-evaluated as the parameters evolve.

Table 2: Summary of the toy-model ROMs obtained by AS-MBAM. RMSE is reported on the same total-error scale as in Fig. 4. Local models are those for which the matrix diffusion constant ω vanishes; non-local models retain a nonzero ω.

Model label	**#param.**	**Local?**	**RMSE**	**Reduction signature**
`M0` (starting point)	7	no	0.015–0.025	(3L+1)pTROM, $L = 2$
`M0-dir1-dir1-dir2`	4	no	0.032	$\beta\cdot\omega^M \to c$ at i_1 and at i_2
`M0-dir1-dir2-dir2`	4	no	0.033	$\beta_{i_2}\cdot\omega^M_{i_2} \to c_2$; $c_1/\omega_{i_1} \to c$
`M0-dir2-dir2-dir1`	4	yes ($\omega \to 0$)	0.023	local model, Eqs. (21)–(22)
`M0-dir2-dir2-dir2-dir1`	3	yes ($\omega \to 0$)	0.028	further reduction: $\beta_{i_1} \to 0$

tree is a data-driven exploration of the boundary complex of the model manifold—the Hasse diagram of limiting theories described by Quinn *et al.* [31]—of which a chain traverses a single path. This multiplicity motivates retaining alternative candidates when the reduced parameters are intended for physical interpretation or health monitoring.

5.5. Selection of a Robust Local Model and Scope of the Reduction

A key insight from the systematic reduction is the identification of an accurate composite *local* (i.e., $\omega \to 0$) ROM with substantially reduced parameter ambiguity, namely model `M0-dir2-dir2-dir1`. The data-driven reduction path associated one with sensor i_1 and the other with i_2, resulting in the following distinct governing equations for the matrix temperatures:

$$\frac{dT^M_{i_1}}{dt} = \omega^M_{i_1}\beta_{i_1}\int_0^t I_{i_1}(\tau)d\tau - \omega^M_{i_1}T^M_{i_1} \tag{21}$$

$$\frac{dT^M_{i_2}}{dt} = c_2\int_0^t I_{i_2}(\tau)e^{-\omega_{i_2}(t-\tau)}d\tau \tag{22}$$

The matrix-coupling parameter ω is soft under the available sensor data: changes in its effect can be compensated by other parameters with little change in accuracy. The hierarchy accordingly contains accurate local and non-local candidates, including `M0-dir1-dir1-dir2` (RMSE=0.032) with nonzero ω. For the target health-monitoring appli-

cation, we select the local candidate because it supports modular, scalable, per-sensor estimators with independent local matrix states.

Direct fits of both local forms, Eqs. (21) and (22), to the synthetic record at each sensor showed comparable accuracy. The two forms therefore represent alternative local simplifications of the toy-model data. We carry Eq. (21) forward as the representative local structure for X-57 evaluation. Its extension from the one-dimensional toy model to the two-dimensional sub-module is a modeling hypothesis motivated by the cell-to-matrix renormalization argument of Section 5.1: contributions from unmeasured cells are absorbed into effective parameters at each sensor location. The pack-wide fits below test the adequacy of that hypothesis for the available X-57 SFP. Transfer across additional topologies and loading profiles will be evaluated in subsequent studies.

6. Pack-wide Evaluation with X-57 Data

6.1. Per-Sensor Model and Resolution of Structural Non-Identifiability

For the X-57 pack-wide evaluation we work *per sensor*: each thermal sensor on each brick is fitted with its own local model, with no parameters shared across sensors or bricks. We select the first of the two interchangeable local thermal models, Eq. (21), and couple it to the electrochemical model of Section 4.2 (Eqs. (10)–(12)). The resulting per-sensor model has eight parameters: the electrochemical parameters A, B_c, B_a, $\tilde{r}$, $N_{Li,a}$ and τ_a, and the two local thermal parameters $\alpha \equiv \omega^M \beta$ and $\tau \equiv 1/\omega^M$. The initial condition $A + B_c = V(0)$, with $V(0)$ the known voltage of a fully charged cell, fixes B_c and leaves seven independent parameters. The first temperature sample of each record is corrupted and is discarded; the second sample defines the reference $T^M(0)$, and the fitted thermal output is the local temperature rise $\Delta T^M(t) \equiv T^M(t) - T^M(0)$, so that

$$\frac{d\Delta T^M}{dt} = \alpha \int_0^t I(t')\, dt' - \frac{1}{\tau}\Delta T^M. \tag{23}$$

All X-57 fits use the first 2060 s of each record, resampled to 300 uniform points, and the Nelder–Mead algorithm with initial parameters drawn uniformly within $\pm 60\%$ of a nominal vector; Section S4 of the SI gives the details. Two properties of this per-sensor model are established in Section S4 of the SI and carried forward here. First, in the absence of direct cell-current measurement the model is structurally non-identifiable under the scaling $N_{Li,a} \to cN_{Li,a}$, $\tilde{r} \to \tilde{r}/c$, $\alpha \to \alpha/c$, which rescales the predicted current and leaves the predicted temperature unchanged. Adding a small-weight normalized current residual to the cost, with the brick-average current as a proxy for the local cell current, breaks this invariance, and multi-start fits at two different small weights return the same parameter distributions. Second, the anode diffusion time constant τ_a is driven to values orders of magnitude below any resolved thermal timescale, because the fitted outputs are insensitive to solid-phase diffusion: the temperature, which dominates the cost, integrates the current, and the weakly weighted brick-average current proxy does not resolve diffusion transients. The limit $\tau_a \to 0$ is therefore a data-driven boundary of the model manifold induced by the information content of the measurements. In this limit the anode surface fraction follows the bulk, and both normalized fractions reduce to the Coulomb-counted value $1 - Q(t)/(eN_{Li,a})$, with $Q(t) = \int_0^t I(t')\, dt'$; hence $\bar{x}_a(t) = \bar{x}_c(t)$, and the model reduces to a six-parameter ROM (A, B_a, $\tilde{r}$, $N_{Li,a}$, α, τ) whose minimum RMSE increases only from 0.006 to 0.007. This six-parameter ROM remains sloppy in the thermal parameters α and τ and in B_a, and it is the starting point for the AS-MBAM continuation of the next section.

6.2. 5-parameter ROM

We applied the general AS-MBAM construction of Eq. (20) to a representative local best fit for one brick and one temperature sensor. At this stage the local ROM contains no cross-sensor coupling, so one representative sensor is sufficient for candidate-structure generation; the two coupled sensor outputs had already been used in the preceding toy-model reduction that established the local ROM. For the X-57 continuation, the physical parameter vector is

$$p_{\mathrm{X57}} = [A, B_a, \tilde{r}, N_{Li,a}, \alpha, \tau]^\top, \qquad q_i = \frac{p_i}{p_{0,i}}. \tag{24}$$

The normalized sensitivity metric combines the local temperature and current channels using their measured root-mean-square magnitudes, with temperature weight one and current weight $(0.03)^2 = 9 \times 10^{-4}$. The plotted trajectory

error is a separate temperature-only diagnostic. The exact discrete definitions are given in Section S3.5 of the SI. We explored both orientations of the softest relative-coordinate mode.

Along the retained branch, the thermal parameters approached

$$\alpha \to \infty, \qquad \tau \to 0, \qquad \gamma = \alpha\tau = \text{finite}. \tag{25}$$

In terms of $Q(t)$ and $\gamma = \alpha\tau$, the thermal equation of the six-parameter ROM, Eq. (23), becomes

$$\tau \frac{d\Delta T}{dt} + \Delta T = \gamma Q(t). \tag{26}$$

Equation (26) still contains both τ and γ; the limit $\tau \to 0$ at fixed γ in Eq. (25) removes τ and the relaxation state and leaves five parameters. This is a fast-state singular-perturbation limit. Its engineering significance is direct: the unresolved internal thermal-relaxation state disappears from the governing equations, the parameter count decreases by one, and the retained composite parameter γ carries the observable thermal gain into the limiting model. The temperature-only trajectory diagnostic rises from approximately 0.007 to approximately 0.014 and then remains nearly flat over the observed continuation, so the limiting structure retains acceptable fit accuracy with a modest increase in that diagnostic. We derived the limiting model analytically, refitted it in a separate optimization, and then evaluated the common model form across the available X-57 brick–sensor records.

Within the explored continuation range, the opposite branch reached the adopted error threshold before approaching an interpretable limiting form and was therefore terminated (both branches are shown in Fig. S2 of the SI). Extending that branch beyond the present range is a possible future search. The X-57 reduction therefore retained a single accepted branch at this level: the branch enumeration yielded one accepted and one terminated candidate, and the resulting reduction is a chain. The branching search is demonstrated in full on the toy model of Section 5.4, where several accepted children were retained and propagated (Table 2). Whether a larger X-57 candidate tree exists under other coordinates, acceptance criteria, or continuation ranges is left to the searches proposed above.

The analytical limit of Eq. (26) gives $\Delta T = \gamma Q$ and yields the five-parameter Thermal Reduced-Order Model (5pTROM):

$$I(t) = \frac{A + (V(0) - A)\bar{x}_c(t) + B_a \log \bar{x}_c(t) - V(t)}{\tilde{r}} \tag{27}$$

$$\frac{d\bar{x}_c}{dt} = -\frac{I(t)}{eN_{Li,a}} \tag{28}$$

$$\Delta T(t) \equiv T(t) - T(0) = \gamma \int_0^t I(t')dt'. \tag{29}$$

For the pack-wide 5pTROM fits, the corrupted initial temperature samples are handled by replacing the values recorded during the first 10 s with the value at 10 s, which defines the reference $T(0)$. In the preceding $\tau_a \to 0$ reduction, $\bar{x}_a(t) \to \bar{x}_c(t)$, so the 5pTROM is naturally written in terms of the single intercalation variable $\bar{x}_c(t)$. The parameter τ eliminated in Eq. (25) is an internal effective cell-to-matrix relaxation time. It is distinct from the external sub-module cooling time $\tau_{\text{ext}} \approx 6.7$ h, which supports the quasi-adiabatic external boundary condition.

The model gives a data-consistent interpretation of the observable local temperature rise as proportional to charge throughput, with γ representing the effective temperature rise per unit charge. This interpretation belongs to the retained candidate evaluated here; alternative data-consistent structures may represent the same observations.

6.3. Estimation of 5pTROM from X-57 data

The candidate five-parameter structure was generated from one representative local fit for one brick and one temperature sensor. This single-sensor continuation is appropriate because the local ROM obtained from the two-output toy-model reduction no longer couples the sensor predictions. The selected structure was then refitted separately for every brick–sensor pair, providing a pack-wide test of fit accuracy and diagnostic resolution.

Pack-wide thermal response and residual structure. Figure 6 evaluates the 5pTROM fit quality over all 256 separately optimized brick–sensor pairs. Panel (a) shows the measured temperatures in their original, unzeroed units. The traces exhibit an initially nearly isothermal interval, heating during the high-power portion of the SFP discharge, a peak or transition region near 1200 s to 1400 s, and a late-time plateau or relaxation regime. The spread across bricks and sensors motivates the per-brick, per-sensor estimation strategy.

Panel (b) overlays the temperature residuals $e_T(t) \equiv T_{\text{pred}}(t) - T_{\text{meas}}(t)$ for the same fits. The sensor-specific heat maps in panels (c) and (d) resolve their temporal structure across brick number. Both sensors exhibit an early positive band, a broad negative band near 1300 s to 1500 s, and a weaker late positive band. This cross-sensor coherence identifies a systematic component in the model–data discrepancy. Its timing suggests sensitivity to SFP load transitions or omitted transient thermal dynamics. Horizontal streaks localize the largest deviations to a small number of brick–sensor pairs.

Absolute residual statistics. Figure 7 quantifies the residual magnitude for each brick–sensor fit in physical temperature units. For N_t fitted time samples, the absolute temperature root-mean-square error is $\text{RMSE}_T = [N_t^{-1} \sum_k e_T^2(t_k)]^{1/2}$. For most fits, RMSE_T is approximately 0.3 °C to 0.5 °C, and the 95th percentile of $|e_T|$ is below about 1 °C. A small number of fits have substantially larger errors; these cases correspond to the horizontal streaks and largest excursions in Fig. 6. The present metrics report the physical temperature-error scale; normalized, dimensionless RMSE remains the model-comparison convention elsewhere in the paper. The 95th-percentile and maximum measures characterize the upper-tail magnitude and isolated extrema, respectively. Figures 6 and 7 establish the pack-wide error scale and localize the largest deviations by brick, sensor, and time. These resolved deviations provide fit-quality diagnostics and candidate inputs for anomaly-detection studies using repeated-use or fault-labeled data.

Population analysis across all 128 bricks. With the pack-wide fit accuracy and residual structure established, we now use the 5pTROM parameter estimates to characterize brick-to-brick heterogeneity across the X-57 battery pack. For each of the 128 bricks and each of the two sensors, a ten-start optimization was performed to find the best-fit values for the five model parameters: A, B_a, $\tilde{r}$, $N_{Li,a}$, and γ; the start with the lowest cost was retained. The results of this comprehensive fitting procedure are summarized in Figure 8.

The fitted parameters vary across the brick population. Four parameters—A, $\tilde{r}$, $N_{Li,a}$, and γ—show smooth, spatially organized trends with brick number, including a pronounced variation in the effective resistance $\tilde{r}$. Because brick number maps to physical position within the pack, these trends are consistent with location-dependent electrical and thermal response. Future joint analysis of pack heterogeneity, sensor calibration, and systematic model discrepancy will sharpen the physical attribution of these spatial trends.

The parameter B_a shows weak spatial coherence and large adjacent-brick scatter. Its local variation is comparable to its variation across the pack, consistent with practical non-identifiability under the available data. Accordingly, B_a is excluded from spatial physical interpretation for this dataset.

These results support retaining the 5pTROM as the terminal candidate for the present application. Four fitted parameters per sensor—A, $\tilde{r}$, $N_{Li,a}$, and γ—show coherent spatial trends, whereas B_a remains visibly sloppy. Future uncertainty analysis will quantify confidence in the four retained features. The explored branch terminates at the 5pTROM while preserving its mechanism-linked structure; additional searches using other coordinates, datasets, and candidate families will test alternative four-parameter forms.

The 5pTROM therefore provides four spatially resolved retained fitted features per sensor and identifies B_a as the remaining practically sloppy parameter for the present SFP dataset.

6.4. Diagnostic Feature Yield and Interpretation of the 5pTROM

The practical value of the systematic reduction can be illustrated by comparing the fitted or directly derived diagnostic quantities available from the X-57 telemetry with those maintained in a typical battery-management workflow. The present comparison quantifies diagnostic feature yield; future work will quantify information-theoretic and decision-level value.

A typical battery health monitoring workflow treats voltage and temperature with loosely coupled lumped models [11, 47]. On the electrical side, a first- or second-order equivalent-circuit model [11, 14] adapts a few scalars online from cycling data—at minimum an ohmic/internal resistance and a usable-capacity estimate; many stacks also maintain one transient-response (voltage-relaxation) component, adding a gain and a time constant [14]. On the thermal

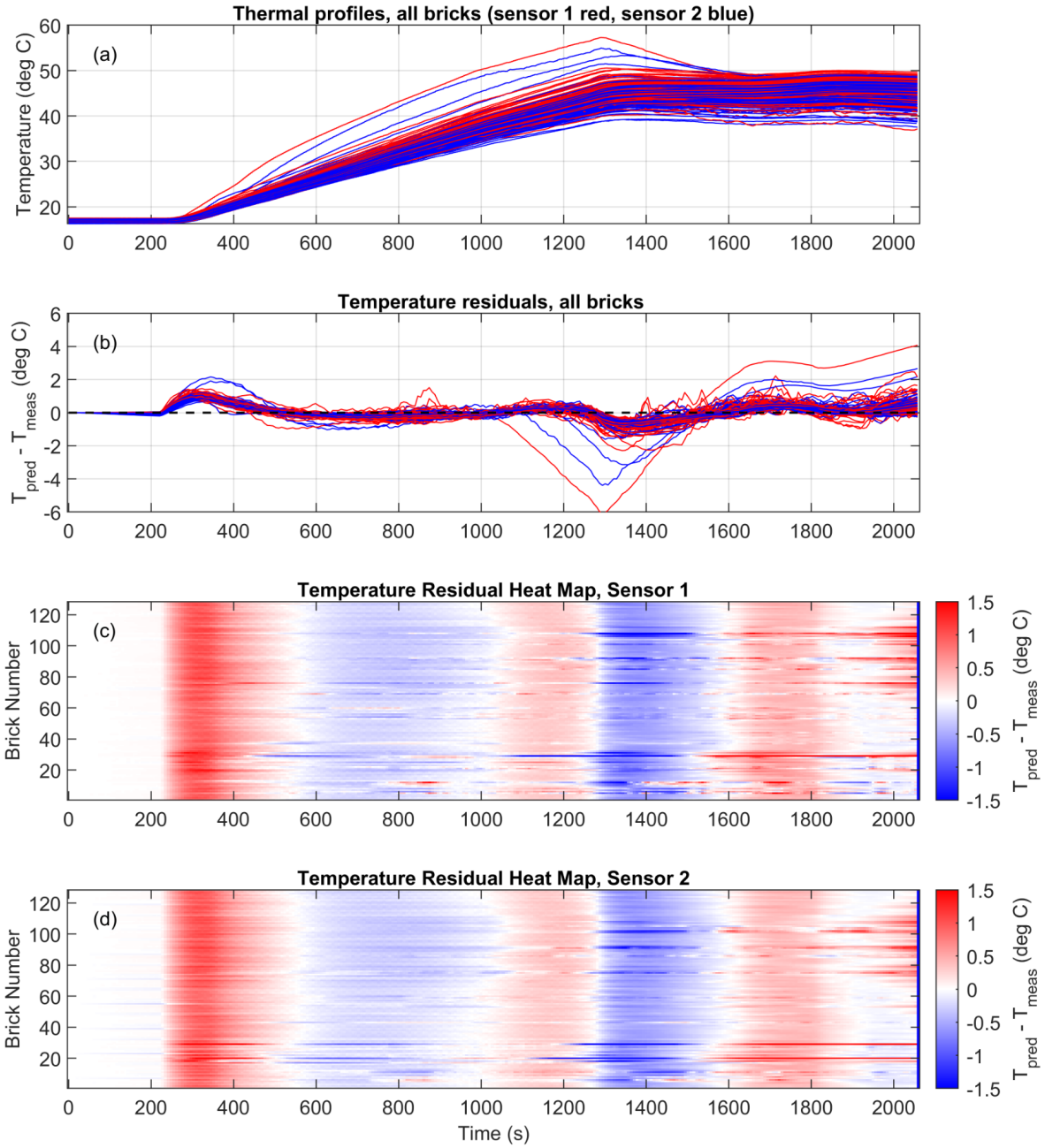


Figure 6: Pack-wide thermal response and 5pTROM temperature residuals during the SFP discharge. **(a)** Measured temperatures for all 128 bricks in the original temperature frame; sensor 1 is red and sensor 2 is blue. **(b)** Residuals $e_T = T_{\text{pred}} - T_{\text{meas}}$ for the 256 separately fitted brick–sensor pairs. **(c,d)** Residual heat maps for sensor 1 and sensor 2, respectively. Red denotes model overprediction, blue denotes underprediction, and white denotes a near-zero residual. The heat-map scale is clipped at $\pm 1.5\,^{\circ}\text{C}$; values outside this range are saturated. All panels share the same time axis.

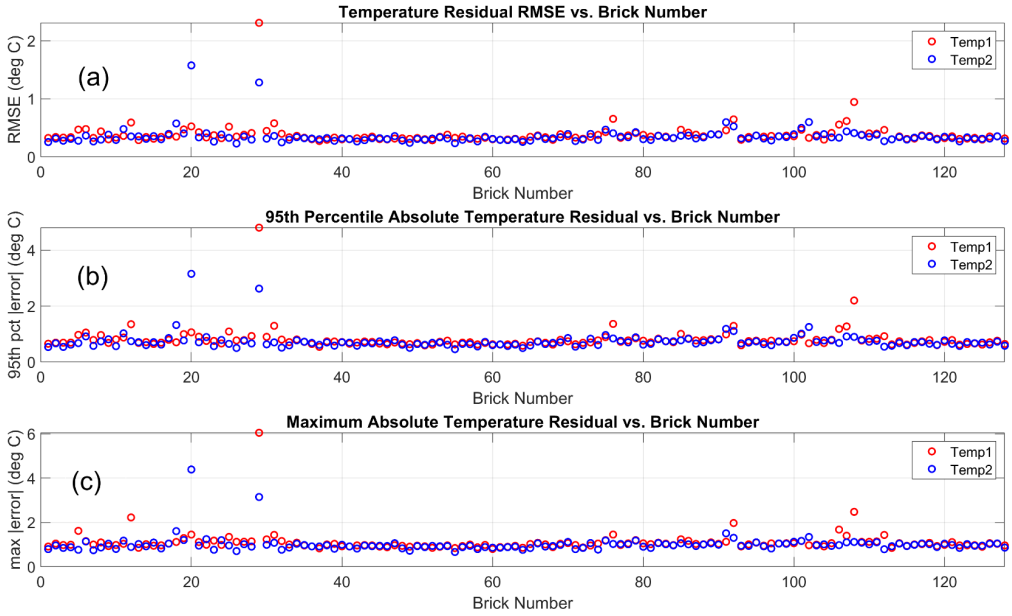


Figure 7: Absolute temperature-residual statistics for the 5pTROM fits as a function of brick number. Red open circles denote sensor 1 and blue open circles denote sensor 2, consistent with Fig. 6. Metrics are computed over the fitted SFP time samples for each brick–sensor pair. **(a)** Absolute temperature RMSE, RMSE_T. **(b)** The 95th percentile of $|e_T|$. **(c)** The maximum of $|e_T|$. All quantities are reported in degrees Celsius.

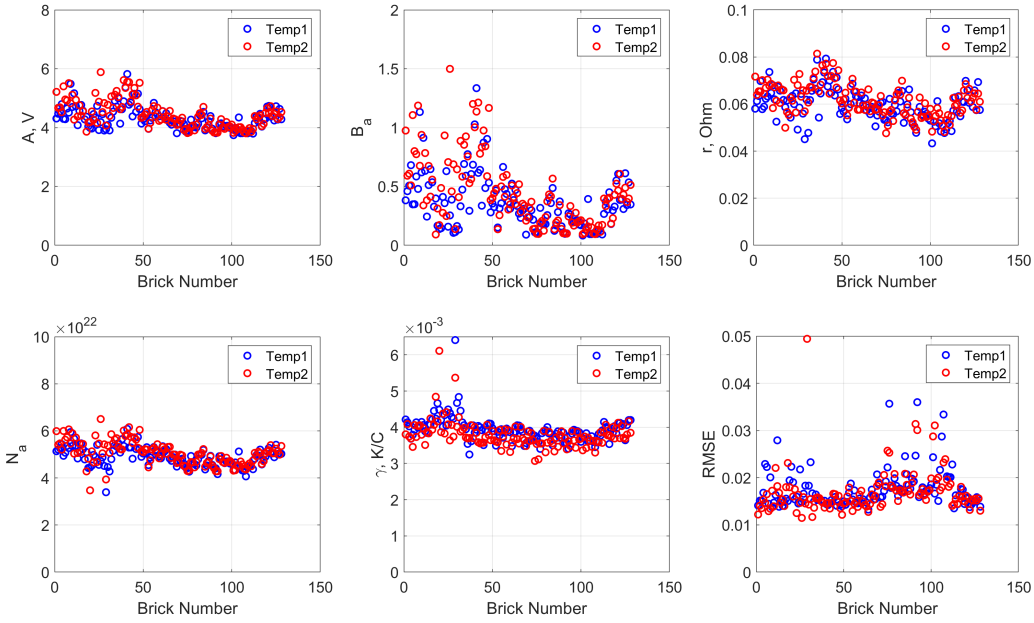


Figure 8: Best-fit parameters of the 5pTROM for all 128 bricks of the X-57 battery pack. Each panel shows one fitted parameter versus brick number; blue and red circles correspond to the two temperature-sensor fits. The smooth variation of A, $\tilde{r}$, $N_{Li,a}$, and γ is consistent with spatially organized electrical and thermal response. The weak spatial coherence and large local scatter of B_a are consistent with practical non-identifiability under the available data.

side, each temperature sensor is handled with a per-sensor temperature-rise coefficient or an equivalent one-lump thermal parameter [47]. Pre-calibrated look-up maps, for example versus state of charge and temperature, supply the remaining elements [47–49]. In practice, this yields on the order of $\sim$3–6 effective, empirically maintained scalars per brick from field data.

The 5pTROM begins from a coupled physics-based electro–thermal description and reduces it systematically to a compact parameterization with four retained fitted parameters per sensor (A, $\tilde{r}$, $N_{\mathrm{Li},a}$, and γ) that exhibit coherent pack-wide trends under the available sensing. The two temperature-sensor fits therefore provide eight reported fitted features per brick. Because both fits reuse the same brick-level voltage and current record and may share common model discrepancy, these features form a correlated diagnostic set with sensor-specific thermal information. Coulomb counting adds a separate direct estimate of usable capacity.

The present dataset shows that the reduced model exposes a larger set of spatially resolved, mechanism-linked candidate health indicators from the available V/I/T channels than a conventional loosely coupled workflow typically maintains online. Repeated missions, aging evolution, and fault-labeled data will enable subsequent studies to quantify information-theoretic gain and test whether these additional features improve fault classification, aging-state estimation, and prognosis.

7. Conclusions

This work applies systematic physics-based model reduction to construct a compact thermal estimator for the NASA X-57 Maxwell Li-ion battery pack. The comprehensive HFM contains nearly 1300 independent parameters, while sparse spatial sensing, structural degeneracies, and strongly sloppy sensitivity directions leave many parameter combinations weakly observable. This mismatch between model detail and observable parameter combinations motivates the staged reduction.

The first methodological contribution of this work is AS-MBAM. Standard MBAM locates limiting models by integrating a geodesic of the FIM-induced metric, an update that requires the directional second derivative of the model outputs at every step. AS-MBAM advances the continuation by re-evaluating the softest first-order sensitivity direction, so the search runs on the Jacobian already computed for fitting and identifiability analysis, with no second-order derivative information required. Launching the continuation from both orientations of the soft mode at every retained model generates a branching tree of candidate limits, and each candidate is derived analytically and refitted independently before it is accepted. AS-MBAM was designed for the engineering setting in which MBAM has so far seen little use: the Jacobian and its FIM eigendecomposition serve fitting, identifiability reporting, and candidate discovery alike, so systematic manifold-boundary reduction can be carried out inside an identifiability analysis that an engineering model already requires.

The second contribution is the staged reduction chain in which AS-MBAM is embedded. Physics-guided coarse graining first reduces the nearly-1300-parameter HFM to a sensor-scaled model, and the soft-mode boundary search then operates on tractable local ROMs. The retained X-57 branch approaches $\alpha \to \infty$ and $\tau \to 0$ with $\alpha\tau = \gamma$ finite, yielding the five-parameter Thermal Reduced-Order Model (5pTROM). In the information-geometric sense emphasized by Quinn *et al.*, this boundary identifies dynamics unresolved by the present forcing and observations and defines an experiment-specific effective theory.

Pack-wide evaluation on one laboratory SFP discharge shows that the same 5pTROM form fits the 256 brick–sensor temperature records with absolute RMSE of approximately 0.3 °C to 0.5 °C for most fits and a 95th-percentile absolute residual below about 1 °C. Residual heat maps reveal a coherent pack-wide discrepancy near SFP transitions, identifying a systematic component of model error. Four fitted parameters per sensor exhibit spatially organized trends, whereas B_a remains practically non-identifiable. These quantities are mechanism-linked diagnostic features whose physical attribution depends on sensor calibration, the local-current approximation, and systematic model discrepancy. The retained thermal relation $\Delta T = \gamma \int I\,dt$ is a data-consistent effective description specific to the tested quasi-adiabatic SFP regime.

The present work establishes within-profile fit accuracy, a common pack-wide model form, and a practical staged route from detailed physics to a compact estimator with substantially reduced parameter ambiguity relative to the preceding model stages. Future work will test cross-mission parameter transfer, anomaly-detection performance, prognostic value, and transfer to other battery architectures and thermal-management regimes using repeated-use, aging, fault-labeled, and alternative-cooling datasets.

Data availability

The data and code supporting this study are available from the corresponding author upon reasonable request.

Acknowledgements

This work was supported by the NASA Transformational Tools and Technologies (TTT) project. The authors thank David Mebane for many fruitful discussions, and Katelyn Jarvis Griffith for her contributions to the earlier stages of this work. The authors also thank Sean Clarke and his co-authors of Ref. [39] for permission to reproduce the CAD renderings in Fig. 1.

References

[1] L. Tang, A. Saxena, K. Younsi, Prognostics and Health Management for Electrified Aircraft Propulsion: State of the Art and Challenges, Journal of Engineering for Gas Turbines and Power 147 (4) (2025) 041018. doi:10.1115/1.4066598.

[2] A. Barzkar, M. Ghassemi, Components of Electrical Power Systems in More and All-Electric Aircraft: A Review, IEEE Transactions on Transportation Electrification 8 (4) (2022) 4037–4053. doi:10.1109/TTE.2022.3174362.

[3] S. Karpuk, A. Elham, Influence of Novel Airframe Technologies on the Feasibility of Fully-Electric Regional Aviation, Aerospace 8 (6) (2021) 163. doi:10.3390/aerospace8060163.

[4] R. E. Wolleswinkel, R. De Vries, M. Hoogreef, R. Vos, A New Perspective on Battery-Electric Aviation, Part I: Reassessment of Achievable Range, in: AIAA SCITECH 2024 Forum, American Institute of Aeronautics and Astronautics, Orlando, FL, 2024. doi:10.2514/6.2024-1489.

[5] V. Viswanathan, A. H. Epstein, Y.-M. Chiang, E. Takeuchi, M. Bradley, J. Langford, M. Winter, The challenges and opportunities of battery-powered flight, Nature 601 (7894) (2022) 519–525. doi:10.1038/s41586-021-04139-1.

[6] A. R. Gnadt, R. L. Speth, J. S. Sabnis, S. R. Barrett, Technical and environmental assessment of all-electric 180-passenger commercial aircraft, Progress in Aerospace Sciences 105 (2019) 1–30. doi:10.1016/j.paerosci.2018.11.002.

[7] W. L. Fredericks, S. Sripad, G. C. Bower, V. Viswanathan, Performance metrics required of next-generation batteries to electrify vertical takeoff and landing (VTOL) aircraft, ACS Energy Letters 3 (12) (2018) 2989–2994. doi:10.1021/acsenergylett.8b02195.

[8] S. Fu, N. P. Avdelidis, Prognostic and Health Management of Critical Aircraft Systems and Components: An Overview, Sensors 23 (19) (2023) 8124. doi:10.3390/s23198124.

[9] G. W. Vogl, B. A. Weiss, M. A. Donmez, Standards for Prognostics and Health Management (PHM) Techniques within Manufacturing Operations, Proceedings of the Annual Conference of the PHM Society 6 (1) (2014). doi:10.36001/phmconf.2014.v6i1.2503.

[10] H. Meng, Y.-F. Li, A review on prognostics and health management (PHM) methods of lithium-ion batteries, Renewable and Sustainable Energy Reviews 116 (2019) 109405. doi:10.1016/j.rser.2019.109405.
URL https://doi.org/10.1016/j.rser.2019.109405

[11] S. M. Rezvanizaniani, Z. Liu, Y. Chen, J. Lee, Review and recent advances in battery health monitoring and prognostics technologies for electric vehicle (EV) safety and mobility, Journal of Power Sources 256 (2014) 110–124. doi:10.1016/j.jpowsour.2014.01.085.

[12] Y. Jia, L. Brancato, M. Giglio, F. Cadini, Online Core Temperature Estimation for Lithium-Ion Batteries via an Aging-Integrated ECM-1D Coupled Model-Based Algorithm, Batteries 11 (4) (2025) 160. doi:10.3390/batteries11040160.

[13] S. K. Rahimian, S. Rayman, R. E. White, Comparison of single particle and equivalent circuit analog models for a lithium-ion cell, Journal of Power Sources 196 (20) (2011) 8450–8462. doi:10.1016/j.jpowsour.2011.06.007.

[14] M.-K. Tran, A. DaCosta, A. Mevawalla, S. Panchal, M. Fowler, Comparative Study of Equivalent Circuit Models Performance in Four Common Lithium-Ion Batteries: LFP, NMC, LMO, NCA, Batteries 7 (3) (2021) 51. doi:10.3390/batteries7030051.

[15] J. Yao, J. Kowal, A multi-scale data-driven framework for online state of charge estimation of lithium-ion batteries with a novel public drive cycle dataset, Journal of Energy Storage 107 (2025) 114888. doi:10.1016/j.est.2024.114888.

[16] M. Dubarry, G. Baure, C. Pastor-Fernández, T. F. Yu, W. D. Widanage, J. Marco, Battery energy storage system modeling: A combined comprehensive approach, Journal of Energy Storage 21 (2019) 172–185. doi:10.1016/j.est.2018.11.012.

[17] S. E. J. O'Kane, W. Ai, G. Madabattula, D. Alonso-Alvarez, R. Timms, V. Sulzer, J. S. Edge, B. Wu, G. J. Offer, M. Marinescu, Lithium-ion battery degradation: how to model it, Physical Chemistry Chemical Physics 24 (13) (2022) 7909–7922. doi:10.1039/D2CP00417H.

[18] F. Guo, L. D. Couto, G. Mulder, K. Trad, G. Hu, O. Capron, K. Haghverdi, A systematic review of electrochemical model-based lithium-ion battery state estimation in battery management systems, Journal of Energy Storage 101 (2024) 113850. doi:10.1016/j.est.2024.113850.

[19] M. W. Verbrugge, B. J. Koch, Electrochemical analysis of lithiated graphite anodes, Journal of The Electrochemical Society 150 (3) (2003) A374. doi:10.1149/1.1553788.

[20] C. R. Birkl, E. McTurk, M. R. Roberts, P. G. Bruce, D. A. Howey, A parametric open circuit voltage model for lithium ion batteries, Journal of The Electrochemical Society 162 (12) (2015) A2271. doi:10.1149/2.0331512jes.

[21] M. Guo, G. Sikha, R. E. White, Single-particle model for a lithium-ion cell: Thermal behavior, Journal of The Electrochemical Society 158 (2) (2011) A122. doi:10.1149/1.3521314.

[22] M. Andersson, M. Streb, J. Y. Ko, V. Löfqvist Klass, M. Klett, H. Ekström, M. Johansson, G. Lindbergh, Parametrization of physics-based battery models from input–output data: A review of methodology and current research, Journal of Power Sources 521 (2022) 230859. doi:10.1016/j.jpowsour.2021.230859.

[23] A. M. Bizeray, J. Kim, S. R. Duncan, D. A. Howey, Identifiability and parameter estimation of the single particle lithium-ion battery model, IEEE Transactions on Control Systems Technology 27 (5) (2019) 1862–1877. doi:10.1109/TCST.2018.2838097.

[24] Q. Zhang, R. E. White, Comparison of approximate solution methods for the solid phase diffusion equation in a porous electrode model, Journal of Power Sources 165 (2) (2007) 880–886. doi:10.1016/j.jpowsour.2006.12.056.
[25] S. Khaleghi Rahimian, S. Rayman, R. E. White, Extension of physics-based single particle model for higher charge–discharge rates, Journal of Power Sources 224 (2013) 180–194. doi:10.1016/j.jpowsour.2012.09.084.
[26] A. Sharma, H. K. Fathy, Fisher identifiability analysis for a periodically-excited equivalent-circuit lithium-ion battery model, in: 2014 American Control Conference, 2014, pp. 274–280. doi:10.1109/ACC.2014.6859360.
[27] V. Sulzer, P. Mohtat, A. Aitio, S. Lee, Y. T. Yeh, F. Steinbacher, M. U. Khan, J. W. Lee, J. B. Siegel, A. G. Stefanopoulou, D. A. Howey, The challenge and opportunity of battery lifetime prediction from field data, Joule 5 (8) (2021) 1934–1955. doi:10.1016/j.joule.2021.06.005.
[28] M. Khasin, C. S. Kulkarni, K. Goebel, Parameters inference and model reduction for the Single-Particle Model of Li ion cells, arXiv preprint arXiv:1912.05807 (2019). arXiv:1912.05807.
[29] M. Khasin, M. R. Mehta, C. Kulkarni, J. W. Lawson, Thermal data-driven model reduction for enhanced battery health monitoring, Journal of Power Sources 604 (2024) 234442. doi:10.1016/j.jpowsour.2024.234442.
[30] M. R. Mehta, K. M. Crowley, M. Khasin, C. S. Kulkarni, B. DeMattia, J. W. Lawson, Anomaly detection in Li-ion cells using physics-based reduced-order thermal models, Journal of Power Sources 631 (2025) 236190. doi:10.1016/j.jpowsour.2025.236190.
[31] K. N. Quinn, M. C. Abbott, M. K. Transtrum, B. B. Machta, J. P. Sethna, Information geometry for multiparameter models: new perspectives on the origin of simplicity, Reports on Progress in Physics 86 (3) (2022) 035901. doi:10.1088/1361-6633/aca6f8.
URL https://doi.org/10.1088/1361-6633/aca6f8
[32] M. K. Transtrum, P. Qiu, Model reduction by manifold boundaries, Physical Review Letters 113 (9) (2014) 098701. doi:10.1103/physrevlett.113.098701.
URL https://doi.org/10.1103/physrevlett.113.098701
[33] M. K. Transtrum, B. L. Francis, C. C. Youn, A. T. Saric, A. M. Stankovic, Geometrically motivated reparameterization for identifiability analysis in power systems models, in: 2018 North American Power Symposium (NAPS), IEEE, 2018. doi:10.1109/naps.2018.8600617.
URL https://doi.org/10.1109/naps.2018.8600617
[34] M. K. Transtrum, P. Qiu, Bridging mechanistic and phenomenological models of complex biological systems, PLoS Computational Biology 12 (5) (2016) e1004915. doi:10.1371/journal.pcbi.1004915.
URL https://doi.org/10.1371/journal.pcbi.1004915
[35] D. G. Whittaker, J. Wang, J. G. Shuttleworth, R. Venkateshappa, J. M. Kemp, T. W. Claydon, G. R. Mirams, Ion channel model reduction using manifold boundaries, Journal of the Royal Society Interface 19 (193) (2022) 20220193. doi:10.1098/rsif.2022.0193.
URL https://doi.org/10.1098/rsif.2022.0193
[36] P. E. Paré, D. Grimsman, A. T. Wilson, M. K. Transtrum, S. Warnick, Model boundary approximation method as a unifying framework for balanced truncation and singular perturbation approximation, arXiv preprint arXiv:1901.02569 (2019). doi:10.48550/arXiv.1901.02569.
URL https://arxiv.org/abs/1901.02569
[37] M. Khasin, M. R. Mehta, K. Jarvis Griffith, J. W. Lawson, Systematic Model Reduction for Battery Health Monitoring: A Physics-Based Approach Applied to X-57 Battery Packs, Presentation at the 2024 NASA Aerospace Battery Workshop, Huntsville, Alabama, 19 November 2024 (2024).
[38] M. Fernández-Ruz, I. Jiménez-Serra, M. Castro, M. Ruiz-Bermejo, J. Aguirre, Strong parameter hierarchy in the interstellar phosphorus chemical network, Frontiers in Astronomy and Space Sciences 12 (2025) 1570525. doi:10.3389/fspas.2025.1570525.
[39] D. Hernandez-Lugo, S. Clarke, T. Miller, M. Redifer, T. Foster, X-57 Maxwell Battery from Cell Level to System Level Design and Testing, NASA Technical Reports Server (2018).
URL https://ntrs.nasa.gov/citations/20180005737
[40] C. Forgez, D. Vinh Do, G. Friedrich, M. Morcrette, C. Delacourt, Thermal modeling of a cylindrical LiFePO4/graphite lithium-ion battery, Journal of Power Sources 195 (9) (2010) 2961–2968. doi:10.1016/j.jpowsour.2009.10.105.
[41] G.-H. Kim, A. Pesaran, R. Spotnitz, A three-dimensional thermal abuse model for lithium-ion cells, Journal of Power Sources 170 (2) (2007) 476–489. doi:10.1016/j.jpowsour.2007.04.018.
[42] F. Richter, S. Kjelstrup, P. J. S. Vie, O. S. Burheim, Thermal conductivity and internal temperature profiles of Li-ion secondary batteries, Journal of Power Sources 359 (2017) 592–600. doi:10.1016/j.jpowsour.2017.05.045.
[43] K. O'Regan, F. Brosa Planella, W. D. Widanage, E. Kendrick, Thermal-electrochemical parameters of a high energy lithium-ion cylindrical battery, Electrochimica Acta 425 (2022) 140700. doi:10.1016/j.electacta.2022.140700.
[44] X. Lin, H. E. Perez, J. B. Siegel, A. G. Stefanopoulou, Y. Li, R. D. Anderson, Y. Ding, M. P. Castanier, Online parameterization of lumped thermal dynamics in cylindrical lithium ion batteries for core temperature estimation and health monitoring, IEEE Transactions on Control Systems Technology 21 (5) (2013) 1745–1755. doi:10.1109/TCST.2012.2217143.
[45] R. Bellman, K. J. Åström, On structural identifiability, Mathematical Biosciences 7 (3-4) (1970) 329–339. doi:10.1016/0025-5564(70)90092-X.
[46] L. Ljung, System Identification: Theory for the User, 2nd Edition, Prentice Hall, Upper Saddle River, NJ, 1999.
[47] X. Lin, Y. Kim, S. Mohan, J. B. Siegel, A. G. Stefanopoulou, Modeling and Estimation for Advanced Battery Management, Annual Review of Control, Robotics, and Autonomous Systems 2 (2019) 393–426. doi:10.1146/annurev-control-053018-023643.
[48] S. Lee, J. Cherry, M. Safoutin, J. McDonald, M. Olechiw, Modeling and Validation of 48 V Mild Hybrid Lithium-Ion Battery Pack, SAE International Journal of Alternative Powertrains 7 (3) (2018) 273–287. doi:10.4271/2018-01-0433.
[49] S. Nachimuthu, F. Alsaif, G. Devarajan, I. Vairavasundaram, Real time SOC estimation for Li-ion batteries in Electric vehicles using UKBF with online parameter identification, Scientific Reports 15 (2025) 1714. doi:10.1038/s41598-025-85700-0.